Published OnlineFirst February 11, 2020; DOI: 10.1158/2159-8290.CD-19-0297

RESEARCH ARTICLE

Oncogenic KRAS-Driven Metabolic Reprogramming in Pancreatic Cancer Cells Utilizes Cytokines from the Tumor Microenvironment

Prasenjit Dey[1], Jun Li[2], Jianhua Zhang[2], Surendra Chaurasiya[3], Anders Strom[3], Huamin Wang[4], Wen-Ting Liao[1], Frederick Cavallaro[1], Parker Denz[5], Vincent Bernard[6], Er-Yen Yen[2], Giannicola Genovese[7], Pat Gulhati[1], Jielin Liu[8], Deepavali Chakravarti[1], Pingna Deng[1], Tingxin Zhang[1], Federica Carbone[7], Qing Chang[2], Haoqiang Ying[8], Xiaoying Shang[1], Denise J. Spring[1], Bidyut Ghosh[6], Nagireddy Putluri[9], Anirban Maitra[6], Y. Alan Wang[1], and Ronald A. DePinho[1]

Published OnlineFirst February 11, 2020; DOI: 10.1158/2159-8290.CD-19-0297

ABSTRACT A hallmark of pancreatic ductal adenocarcinoma (PDAC) is an exuberant stroma comprised of diverse cell types that enable or suppress tumor progression. Here, we explored the role of oncogenic KRAS in protumorigenic signaling interactions between cancer cells and host cells. We show that KRAS mutation (KRAS*) drives cell-autonomous expression of type I cytokine receptor complexes (IL2rγ–IL4rα and IL2rγ–IL13rα1) in cancer cells that in turn are capable of receiving cytokine growth signals (IL4 or IL13) provided by invading Th2 cells in the microenvironment. Early neoplastic lesions show close proximity of cancer cells harboring KRAS* and Th2 cells producing IL4 and IL13. Activated IL2rγ–IL4rα and IL2rγ–IL13rα1 receptors signal primarily via JAK1–STAT6. Integrated transcriptomic, chromatin occupancy, and metabolomic studies identified MYC as a direct target of activated STAT6 and that MYC drives glycolysis. Thus, paracrine signaling in the tumor microenvironment plays a key role in the KRAS*-driven metabolic reprogramming of PDAC.

SIGNIFICANCE: Type II cytokines, secreted by Th2 cells in the tumor microenvironment, can stimulate cancer cell–intrinsic MYC transcriptional upregulation to drive glycolysis. This KRAS*-driven heterotypic signaling circuit in the early and advanced tumor microenvironment enables cooperative protumorigenic interactions, providing candidate therapeutic targets in the KRAS* pathway for this intractable disease.

INTRODUCTION

Oncogenic *KRAS* mutation (KRAS*) is a signature genetic alteration in human pancreatic ductal adenocarcinoma (PDAC). Genetically engineered mouse models have validated a critical role of KRAS* in both the initiation and maintenance of PDAC (1–3). KRAS* alone has been shown to cause acinar cell dysplasia or acinar-to-ductal metaplasia (ADM) and, together with inflammatory injury (e.g., cerulein-induced pancreatitis) and/or tumor suppressor deficiencies (e.g., INK4a/ARF, TP53, and/or SMAD4 loss), promotes the malignant transformation of these initiated preneoplastic lesions into high-grade pancreatic intraepithelial neoplasia (PanIN) and frank adenocarcinoma. Most studies to date have focused on cooperative cancer cell–intrinsic oncogenic genetic alterations that drive growth factor–independent proliferation and enhanced survival of cancer cells. In addition, although a growing body of evidence has revealed a key role for cancer-intrinsic oncogenic signals in driving the recruitment of suppressive immunocytes to constrain antitumor immunity, whether and how these infiltrating immunocytes might, in turn, provide additional trophic support for these KRAS*-initiated cancer cells to enable cancer progression is less well defined.

A hallmark feature of PDAC is an extensive desmoplastic stroma comprised of fibroblasts, extracellular matrix (ECM), and immune cells (4–6). Studies have reported both the presence (7, 8) and absence (5, 9) of infiltrating effector immune cells in the PDAC tumor microenvironment (TME), with lymphocyte infiltrates confined mostly to the stromal compartment. The biological relevance of these lymphocytes is suggested by the observation that the presence of a T-cell coinhibitory gene expression pattern is inversely correlated with survival (10). To date, studies exploring the role of lymphocytes in PDAC biology have focused largely on their immunologic functions in constraining tumor initiation and progression. Beyond their role in immune suppression, infiltrating immune cells may also function to support the initiation and growth of PDAC. In the case of $CD4^+$ T cells that are present in malignant lesions (as in this study), some of its subtypes (Th2, Th17, Treg) are known to play critical roles in inflammatory processes in cancer (11, 12), and Th2 subtypes can promote tumor growth via induction of polarization of M1 macrophages into immune-suppressive M2 macrophages (13).

Exploration of the cross-talk between various cells and their factors in the PDAC TME in processes of tumor initiation and progression represents an area of active investigation. Here, we specifically explored the cooperative interactions between mutant-KRAS signaling in cancer cells and cytokines derived from the tumor micronenviroment, specifically infiltrating

[1]Department of Cancer Biology, The University of Texas MD Anderson Cancer Center, Houston, Texas. [2]Department of Genomic Medicine, The University of Texas MD Anderson Cancer Center, Houston, Texas. [3]Center for Nuclear Receptor and Cell Signaling, University of Houston, Houston, Texas. [4]Department of Pathology, Division of Pathology/Lab Medicine, The University of Texas MD Anderson Cancer Center, Houston, Texas. [5]Department of Immunology, Roswell Park Comprehensive Cancer Center, Buffalo, New York. [6]Department of Translational Molecular Pathology, The University of Texas MD Anderson Cancer Center, Houston, Texas. [7]Department of Genitourinary Medical Oncology, The University of Texas MD Anderson Cancer Center, Houston, Texas. [8]Department of Molecular and Cellular Oncology, The University of Texas MD Anderson Cancer Center, Houston, Texas. [9]Department of Molecular and Cellular Biology, Baylor College of Medicine, Houston, Texas.

Note: Supplementary data for this article are available at Cancer Discovery Online (http://cancerdiscovery.aacrjournals.org/).

Current address for P. Dey: Department of Immunology, Roswell Park Comprehensive Cancer Center, Buffalo, New York.

Corresponding Author: Ronald A. DePinho, The University of Texas MD Anderson Cancer Center, 1515 Holcombe Boulevard, Houston, TX 77030. Phone: 832-751-9756; Fax: 713-792-2331; E-mail: rdepinho@mdanderson.org

Cancer Discov 2020;10:608–25

doi: 10.1158/2159-8290.CD-19-0297

Published OnlineFirst February 11, 2020; DOI: 10.1158/2159-8290.CD-19-0297

Th2-polarized CD4$^+$ T cells, in preneoplastic lesions (PanIN) and PDAC. We established that KRAS* drives the expression of cytokine receptors, which are in turn activated by cytokines produced predominantly by infiltrating Th2 cells. Ligand-induced activation of cytokine receptor signals via the JAK–STAT pathway to directly upregulate MYC, which in turn drives metabolic reprogramming by the upregulation of glycolytic genes. This paracrine pathway contributes to KRAS*-driven glycolysis and provides potential therapeutically targetable interactions in the PDAC TME.

RESULTS

KRAS* Upregulates Specific Type I Cytokine Receptor Family Members

The iKRAS* model enables temporal and spatial control of KRAS* in PDAC via doxycycline (Fig. 1A). Upon extinction of mutant KRAS in established tumors, we observed significant rapid changes in the TME, prompting us to explore KRAS*-dependent signaling interactions within and across cancer and host cells (Supplementary Fig. S1A). Gene set enrichment analysis (GSEA) comparisons of KRAS* parental cancer cell lines versus KRAS*-negative relapsed cancer cell lines (KRAS*$^+$ vs. KRAS*$^-$; ref. 3) identified IL2 and IL21 as top oncogenic signature pathways upregulated in the KRAS*$^+$ cell lines (Fig. 1B and C). Similarly, comparison of cell lines "On" versus 24 hours "Off" doxycycline shows enrichment of IL2, IL15, and IL21 gene signatures in the KRAS*-dependent escaper lines (Supplementary Fig. S1B–S1D). We then audited microarray expression patterns of verifiable mouse cytokine genes (~650) in KRAS* "On" versus "Off" cell lines derived from an autochthonous iKRAS* tumor. Among the top 25 KRAS*-upregulated cytokine network genes were IL2Rγ along with one of its family members, IL4rα (Fig. 1D). Finally, meta-analysis of human PDAC identified IL2Rγ as one of the top 50 most overexpressed genes in PDAC tumors (14).

IL2Rγ and IL4R are members of a common gamma chain receptor (γ_c or CD132) family, which is part of a larger superfamily known as the type I cytokine receptor superfamily. IL4 binds to IL4R receptor (CD124; ref. 15), which then recruits the IL2Rγ chain receptor to form a functional type I IL4R receptor (Supplementary Fig. S1E). In addition, IL2Rγ can heterodimerize with the other private coreceptors IL2R, IL7R, IL9R, IL15R, and IL21R to engage the specific cytokines IL2, IL7, IL9, IL15, and IL21, respectively (16). Examination of the type I cytokine receptor family showed that only IL2rγ and IL4rα were regulated by KRAS* (Fig. 1E). Analysis of human PDAC datasets in Oncomine (datasets from following publications: PMIDs 12750293, 15867264, 19732725, and 19260470) also showed IL2Rγ and IL4R overexpression in PDAC relative to normal pancreas (Fig. 1F). Next, we performed digital microdissection of RNA-sequencing (RNA-seq) data of The Cancer Genome Atlas (TCGA) PDAC datasets to identify those cells expressing IL2Rγ and IL4R, which can also be expressed in T cells, macrophages, eosinophils, and basophils. This approach enabled assignment of the source of IL2Rγ to cancer cells and its correlation with mutant-KRAS expression (Supplementary Fig. S1F). Examination of human PDAC samples (n = 121) showed that approximately 95% of patients variably overexpress low to high levels of IL2Rγ and IL4R relative to normal tissues (Fig. 1G and H). Thus, these type I cytokine receptor family members are consistently upregulated in mutant KRAS–expressing human and murine PDAC.

IL4Rα and Not IL2Rγ Contributes to PDAC Progression *In Vivo*

IL2Rγ and IL4Rα are overexpressed in PDAC, where their expression is KRAS* dependent (Fig. 2A; Supplementary Fig. S2A and S2B). Notably, although IL2Rγ gene expression is not necessary for *in vitro* cell proliferation (Fig. 2B and C; Supplementary Fig. S2C), inhibition of IL2Rγ in an *in vivo* syngeneic orthotopic mouse model caused a modest decrease in tumor burden, albeit with rapid recurrence and thus only a modest survival benefit (median survival 32 days compared with 29 days for control tumor; Fig. 2D; Supplementary Fig. S2D–S2F). Decreased tumor burden aligns with previous reports that shRNA-mediated IL2Rγ depletion provokes tumor regression (17). These modest antitumor results raised the possibility that either IL2Rγ plays a marginal role in tumor growth, or an alternate receptor complex or pathway is available to sustain growth and survival signals. Along these lines, the IL4Rα receptor can engage the IL4 ligand via two distinct receptor complexes, type I and II IL4Rα receptors, depending on its dimerization partner. Both type I (IL2Rγ and IL4Rα) and type II (IL4Rα and IL13Rα1) can bind with IL4 and activate its downstream JAK–STAT pathway; however, each complex utilizes distinct JAK kinases and STAT transcription factors (Fig. 2E). We therefore tested and determined that both IL4Rα (Fig. 1F) and IL13Rα1 were indeed regulated by KRAS* (Fig. 2A); specifically, these receptors were among the top 25 cytokine genes regulated by KRAS* (Fig. 1D). The expression of both IL4Rα and IL13Rα1 was lost upon extinction of KRAS* in the iKRAS* mouse model (Supplementary Fig. S2G). We also validated that IL13Rα1 was upregulated in multiple human PDAC tumor datasets compared with PanIN or a nonmalignant part of the pancreas parenchyma (Fig. 2F). In contrast to the modest antitumor impact of IL2Rγ depletion above, shRNA-mediated depletion of IL4Rα led to significant tumor regression and increased survival (median survival 60 days compared with 30 days for control tumor; Fig. 2G and H; Supplementary Fig. S2H and S2I). There was also a significant decrease in the proliferation marker PCNA upon IL4Rα depletion (Fig. 2I). The above findings suggest that IL4Rα is a central node for the dual signaling arising from IL4 or IL13, and contributes to PDAC tumorigenesis.

PDAC Cells Are Responsive to IL4 and IL13 Cytokines Which Drives JAK–STAT–MYC Activation

Thorough analysis of all γ_c cytokine family members (IL2, IL4, IL7, IL9, IL15, and IL21) and IL13 genes revealed that none of the cytokines except IL15 was regulated by KRAS* (Fig. 3A). This led us to speculate that γ_c cytokines may be sourced instead from host cells in the TME. It is well established that ligand-induced dimerization of cytokine receptors leads to cross-phosphorylation of tyrosine residues in JAKs, which in turn interact with the SH2 domain of the STAT transcription factors, leading to STAT phosphorylation, homodimerization, and activation (18). To examine ligand-induced activation and downstream signaling, we systematically analyzed the capacity of the above cytokines to activate any of the four mammalian

Published OnlineFirst February 11, 2020; DOI: 10.1158/2159-8290.CD-19-0297

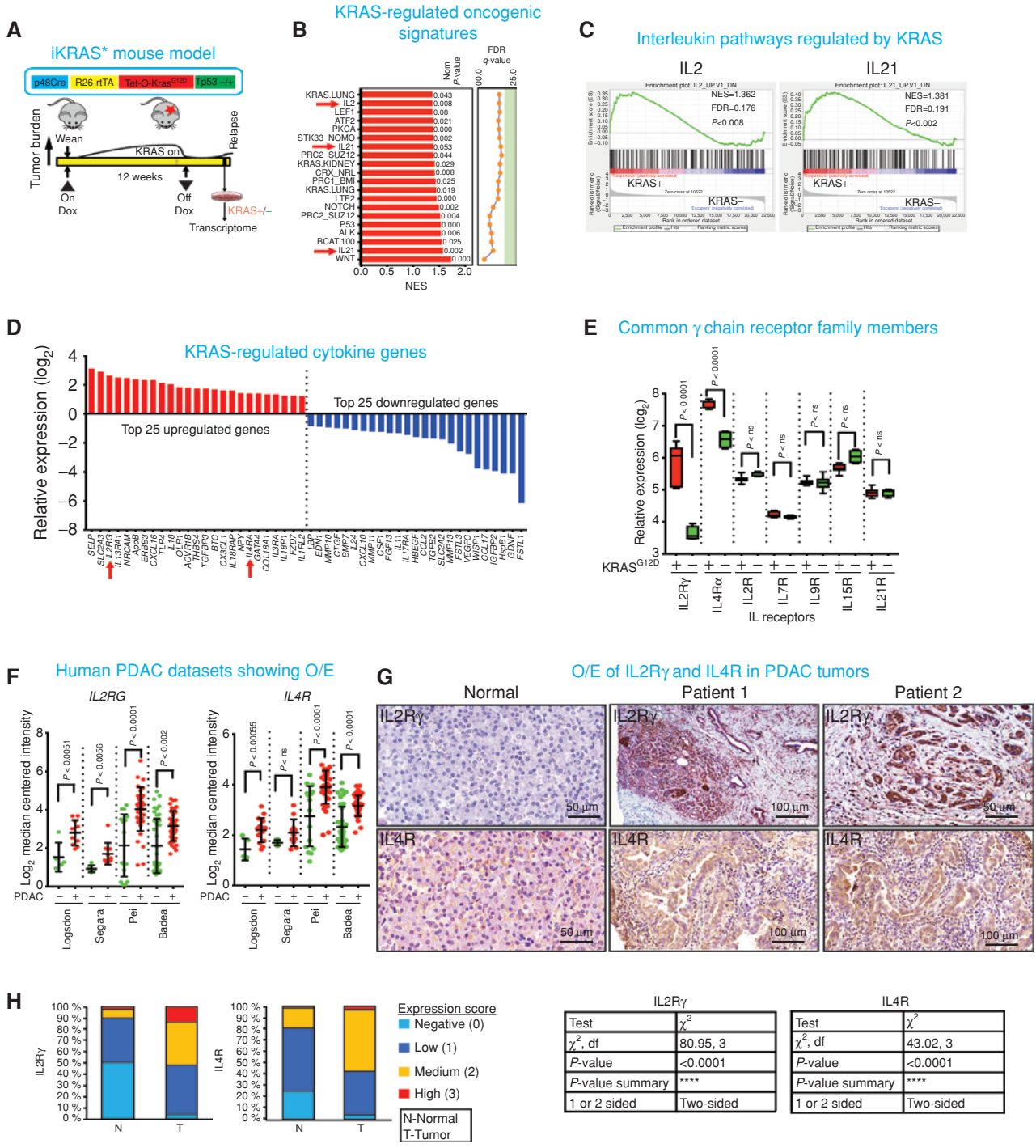

IL2Rγ	
Test	χ^2
χ^2, df	80.95, 3
P-value	<0.0001
P-value summary	****
1 or 2 sided	Two-sided

IL4R	
Test	χ^2
χ^2, df	43.02, 3
P-value	<0.0001
P-value summary	****
1 or 2 sided	Two-sided

Figure 1. KRAS* upregulates specific type I cytokine receptor family members. **A,** Construct of the inducible *KRAS*^{G12D} transgenic mouse alleles (top). Strategy to generate iKRAS* cell lines followed by transcriptome analysis. **B,** GSEA of oncogenic pathways. Pathways of interest IL2, IL15, and IL21 are highlighted in blue and indicated with red arrow. Nominal *P* values (Nom *P*) are shown on the right side of the bar graph. **C,** Graphs showing the enrichment plots generated by GSEA of IL2 and IL21, comparing KRAS$^+$ versus KRAS$^-$ cells. The enrichment score is shown as a scattered green line. In the inset are shown normalized enrichment score (NES), FDR, and Nom *P* value. **D,** Top and bottom 25 mutant KRAS–regulated mouse cytokine family genes. The gene-rank list was generated by manual curation of approximately 650 mouse cytokine genes. **E,** Relative expression of common gamma (γ) chain receptor family genes regulated by KRAS*. Results are shown as mean ± SEM. *P* values were calculated using Student *t* test (ns, not statistically significant). **F,** Differential expression ($\log_2$) of *IL2RG* and *IL4R* genes from human Oncomine datasets. Results are shown as mean ± SEM. *P* values were calculated using Student *t* test (ns, not statistically significant). O/E, overexpression. **G,** Normal (left) and two representative (right two panels) IHC of IL2Rγ and IL4R in human samples ($n = 121$) showing membrane expression of both proteins. Scale bars, 50 μm and 100 μm. **H,** Quantification and statistical analysis of the IHC data from above. Low levels of IL2Rγ and IL4R are expressed in normal pancreas, mostly by the islet cells, whereas medium to high level of expression is observed in PDAC. Statistical analysis of the patient samples is shown in the table to the right of graph.

Published OnlineFirst February 11, 2020; DOI: 10.1158/2159-8290.CD-19-0297

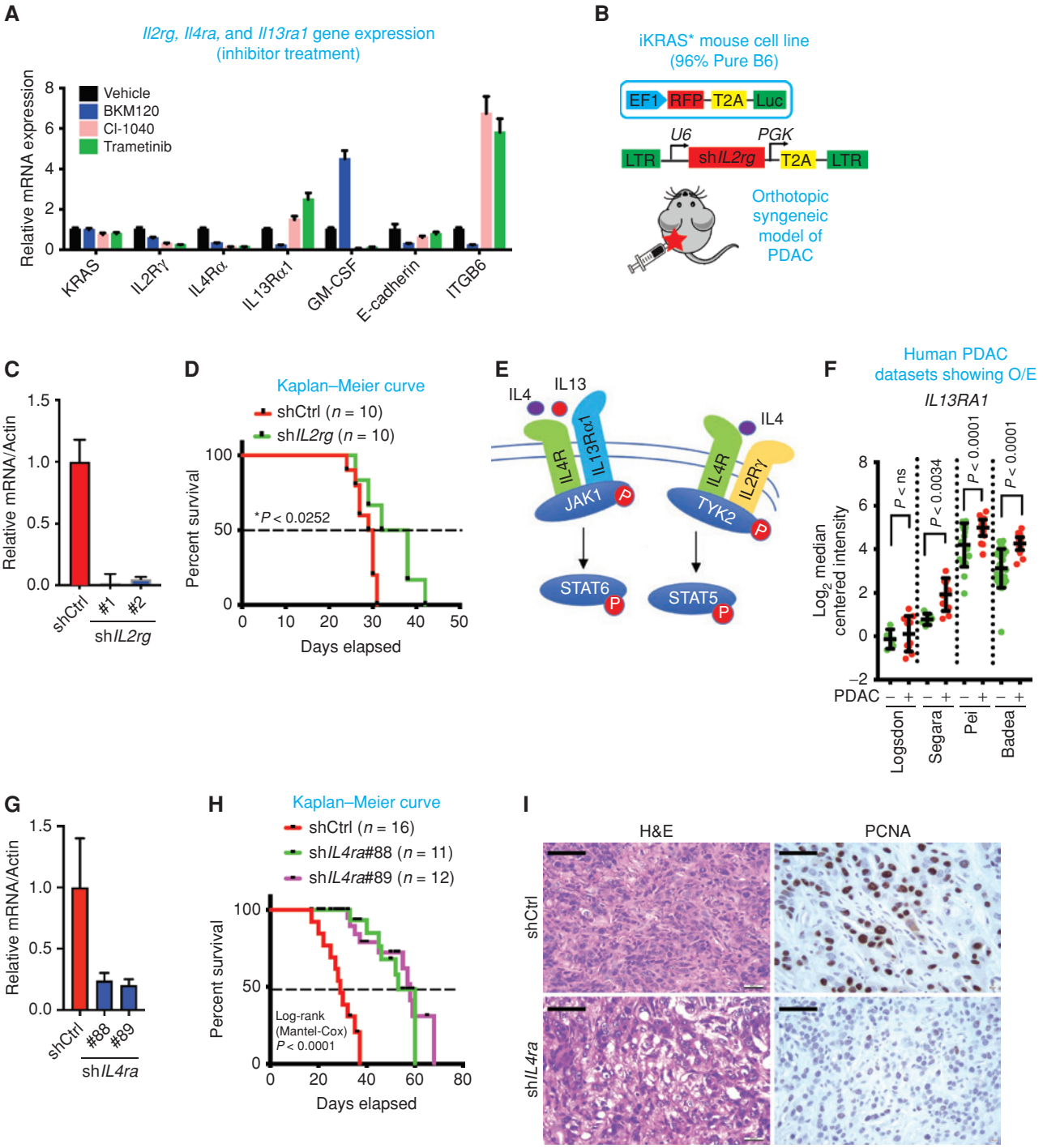

Figure 2. IL4Rα and not IL2Rγ contributes to PDAC progression *in vivo*. **A,** mRNA expression of KRAS, IL2Rγ, IL4rα and IL13Rα1 upon treatment with MEK1/2 (CI-1040 and trametinib) and PI3K (BKM120) inhibitors. Also shown are the mRNA expression of GM-CSF, E-cadherin, and ITGB6, known downstream regulated genes of KRAS and PI3K. **B,** Schematic of the vector construct used to generate luciferase receptor cell lines and shRNA knock-down of IL2Rγ (top). Schematic of orthotopic syngeneic mouse model in C57BL/6 mice (bottom). **C,** mRNA expression of IL2Rγ in mouse tumor cell lines transfected with shRNA for IL2Rγ (clone #1 and #2) or control vector. **D,** Kaplan–Meier survival curves of mice transplanted with mouse tumor cell lines transfected with shRNA for IL2Rγ or control vector ($n = 10$). **E,** Schematic of IL2Rγ–IL4R and IL13Rα1–IL4R pathways. **F,** Differential expression (log_2) of IL13Rα1 in human Oncomine datasets. Results are shown as mean ± SEM. *P* values were calculated using Student *t* test (ns, not statistically significant). O/E, overexpression. **G,** mRNA expression of IL4rα in mouse tumor cell lines transfected with shRNA for IL4Rα (clone #88 and #89) or control vector. **H,** Kaplan–Meier survival curves of mice transplanted with mouse tumor cell lines transfected with sh*IL4ra*#88 ($n = 11$), sh*IL4ra*#89 ($n = 12$), or control vector ($n = 16$). Survival statistics were calculated using log-rank (Mantel–Cox) test; $P < 0.0001$. **I,** Representative hematoxylin and eosin (H&E) and PCNA staining of orthotopic tumor of mouse transfected with sh*IL4ra*#89 or shCtrl cell lines. Scale bars, 50 μm.

Published OnlineFirst February 11, 2020; DOI: 10.1158/2159-8290.CD-19-0297

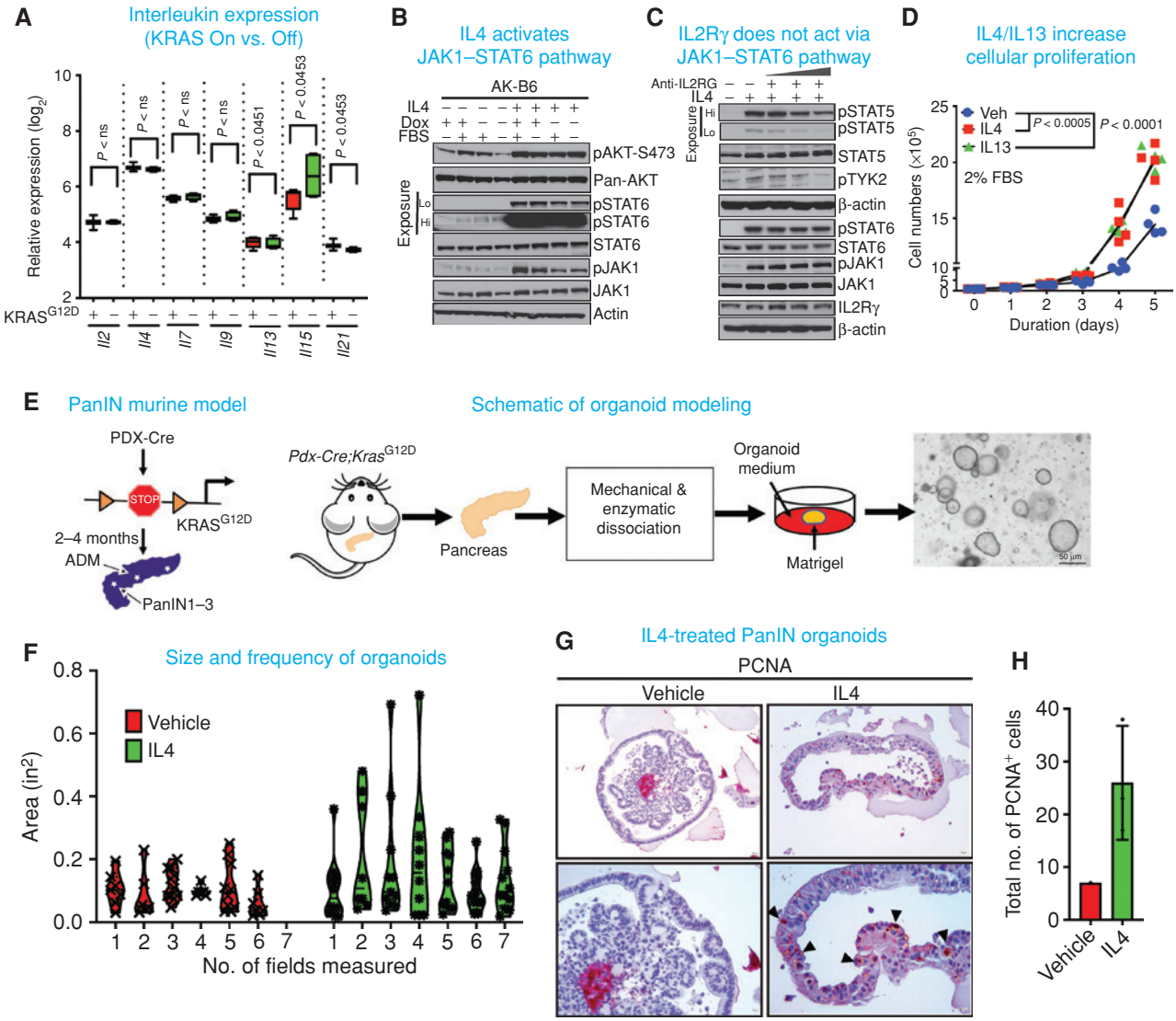

Figure 3. PDAC cells are responsive to IL4 and IL13 cytokines, which drives JAK–STAT–MYC activation. **A,** Relative expression (log_2) of common gamma chain family cytokines On and Off doxycycline (dox). Results are shown as mean ± SEM. *P* values were calculated using Student *t* test (ns, not statistically significant). **B,** Immunoblot analysis for pAKT-S473, pan-AKT, pSTAT6, STAT6, pJAK1, and JAK1 of mouse cell lines treated for 1 hour with IL4 in the presence or absence of FBS and doxycycline. β-actin acts as a loading control. Hi and Lo indicate high and low exposure of the membrane. **C,** Immunoblot analysis for pSTAT5, STAT5, pTYK2, pSTAT6, STAT6, pJAK1, JAK1, and IL2Rγ upon treatment with anti-IL2Rγ (concentration range 3.3, 33, 66, 132 μg/mL, respectively) in the presence or absence of IL4 (10 ng/mL). β-actin acts as a loading control. Hi and Lo indicate high and low exposure of the membrane. **D,** Proliferation assay of mouse cell lines treated with IL4 (10 ng/mL) or IL13 (10 ng/mL) for the days indicated. The cells were cultured in 2% FBS. Data represent $n = 3$, repeated four times. **E,** Schematic of the PanIN mouse model and of the workflow for generating pancreas organoid. **F,** Violin plots of size and frequency of organoids upon treatment with vehicle or IL4. Organoids were grown as droplets in 96-well plates and treated with IL4 (20 ng/mL) for 72 hours. Seven individual wells were imaged and the measurement were done using ImageJ. **G,** Representative IHC of PCNA comparing vehicle and IL4-treated pancreas organoid. **H,** Quantification of PCNA-positive cells following vehicle versus IL4 treatment of organoids. (*continued on next page*)

JAK family members (JAK1, JAK2, JAK3, and TYK2) and the seven STAT family members (STAT1, STAT2, STAT3, STAT4, STAT5a, STAT5b, and STAT6; ref. 18; data not shown). First, we established that IL4-mediated activation of the JAK–STAT pathway was independent of serum status (2% FBS, depletion for 24 hours; Fig. 3B). Second, IL4 and IL13 were the only ligands capable of activating the downstream effectors: specifically, JAK1 (Tyr1034/1035) and TYK2 (Tyr1054/1055) kinases as well as STAT6 (Tyr641) and STAT5 (Tyr694; Fig. 3B; Supplementary Fig. S3A). Consistently, IL4 treatment also activated STAT6 in most human PDAC cell lines tested (Supplementary Fig. S3B). Third, inhibition of IL2Rγ using neutralizing antibodies showed no change in JAK1 or STAT6 phosphorylation, and moderate decrease in pTYK2 and pSTAT5, indicating that IL4 signaling via IL2Rγ–IL4Rα receptors utilized the TYK2–STAT5 pathway, whereas signaling via IL13Rα1–IL4R utilized the JAK1–STAT6 pathway (Fig. 3C). Also, inhibition of IL2Rγ receptor had no effect on IL13 ligand–mediated JAK1–STAT6 activation, indicating that IL13 does not utilize the IL2Rγ–IL4Rα receptor pathway (Supplementary Fig. S3C).

Published OnlineFirst February 11, 2020; DOI: 10.1158/2159-8290.CD-19-0297

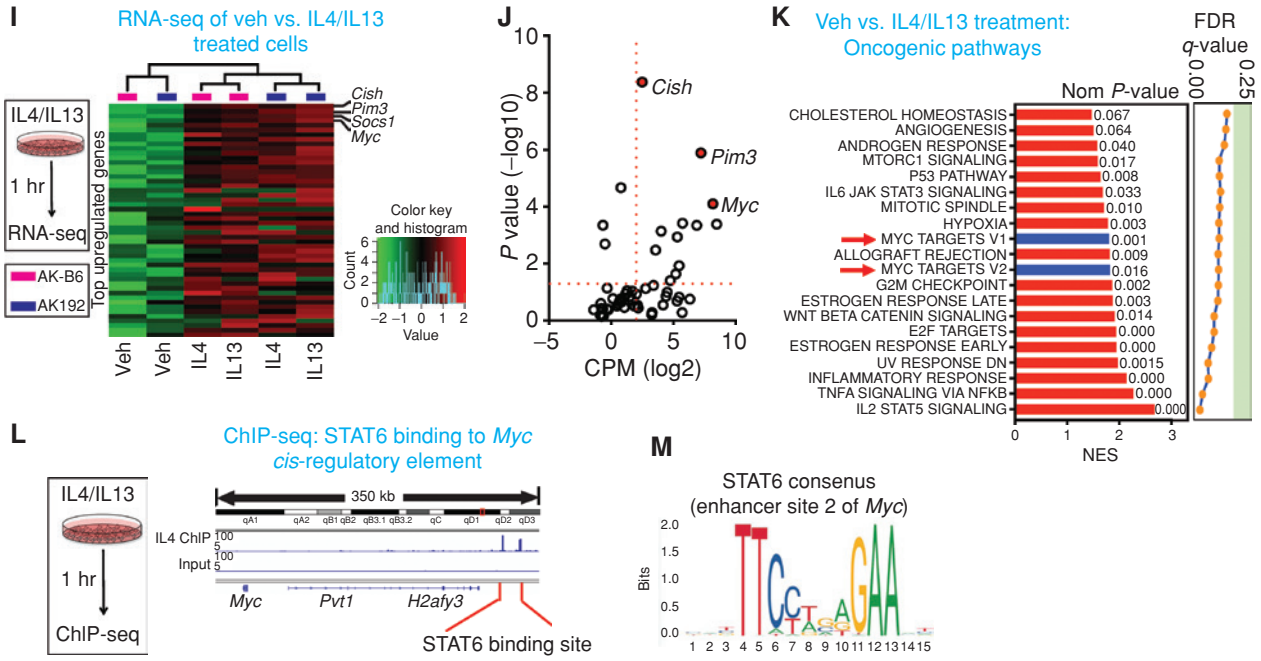

Figure 3. (*Continued*) **I,** Heat maps of the genes enriched in indicated genes upon treatment of cells with IL4 (10 ng/mL) or IL13 (10 ng/mL) for 1 hour. Expression levels shown are representative of $\log_2$ values of each replicate from either vehicle or IL4 treated cultured cell lines. Red signal denotes higher expression relative to the mean expression level within the group, and green signal denotes lower expression relative to the mean expression level within the group. veh, vehicle. **J,** Quantification of the enriched genes based on CPM (log2) versus *P* value ($-\log_{10}$) showing *Myc* as the top enriched gene. **K,** GSEA of oncogenic pathways showing *Myc* as one of the top targets. **L,** ChIP-seq of STAT6 showing binding of STAT6 on the *cis*-element of *Myc*. **M,** Consensus sequence of STAT6 binding site on the *Myc cis*-regulatory element.

This strong activation of the JAK1–STAT6 signaling pathway prompted functional analysis of this pathway on cancer cell survival and tumorigenesis. Specifically, IL4 (10 ng/mL) or IL13 (10 ng/mL) treatment of iKRAS* cell lines increased proliferation (Fig. 3D). To recapitulate the *in vivo* condition, an *ex vivo* organoid model from *Pdx-Cre;LSL-Kras*^{G12D} pancreas was generated (Fig. 3E). Upon characterization, the organoid was identified as being derived from mouse progenitor cells as evidenced by DCLK1 expression and is also positive for epithelial marker, as shown in pan-cytokeratin (Pan-CK; Supplementary Fig. S3D). The established organoids were then tested for response to IL4 treatment, which showed an increase in frequency and size of organoids (Fig. 3F; Supplementary Fig. S3E). Moreover, IL4 treatment led to an increase in staining for the proliferation marker PCNA (Fig. 3G and H). To understand the pro-proliferative actions of IL4 and IL13, RNA-seq analysis was performed, revealing that the top most upregulated genes included *Myc* and *Pim3* (serine/threonine kinase; Fig. 3I and J). Following both IL4 and IL13 treatment, GSEA showed that *Myc* ranked highest among the oncogenic pathways (Fig. 3K; Supplementary Fig. S3F), and the top KEGG pathways were the JAK–STAT pathways (Supplementary Fig. S3G). Given that STAT6 is a transcription factor, chromatin immunoprecipitation sequencing (ChIP-seq) was used to assess whether STAT6 directly binds to the promoter/enhancer regions of the aforementioned genes. ChIP-seq showed that STAT6 bound directly to the enhancer region of these targets (Fig. 3L and M; Supplementary Fig. S3H). As previous work showed that MYC expression has a dose-dependent effect on tumor-cell proliferation (19, 20), the finding that IL4 could elevate *Myc* expression in PDAC cells reinforces the hypothesis of a tumor-promoting role for IL4.

IL4 and IL13 Upregulate MYC to Promote Metabolic Reprogramming

Oncogenic MYC is known to cooperate with KRAS* in driving many cancers and contributes to many cancer hallmarks (21, 22), including cancer cell survival (23, 24), cancer initiation and progression (24, 25), and metabolic reprogramming of bioenergetic pathways such as glutamine (26) and glucose (27) metabolism to support anabolic processes. As our previous work in the iKRAS* model demonstrated an enrichment of MYC E-box binding elements in many genes governing glucose and glutamine metabolism (1), we performed targeted metabolic analysis following a 1-hour treatment of IL4 or IL13 (10 ng/mL) in iKRAS* cells. We observed increased glucose metabolism leading to increased production of pyruvate (Fig. 4A). These findings contrast with earlier *in vitro* studies showing that glucose catabolism in PDAC is directed toward the pentose phosphate pathway (PPP) for synthesis of ribose-5-phosphate (1), and glutaminolysis provides the carbon for the tricarboxylic acid (TCA) cycle. It is interesting to note that *in vivo* metabolism studies in PDAC and other cancer types have definitively shown both glucose and glutamine are utilized by tumors compared to *in vitro* where PDAC cells are mostly dependent on glutamine (28, 29). Thus, we considered the possibility that the presence of cancer cell–extrinsic factors in the TME that include cytokines might contribute to the

Published OnlineFirst February 11, 2020; DOI: 10.1158/2159-8290.CD-19-0297

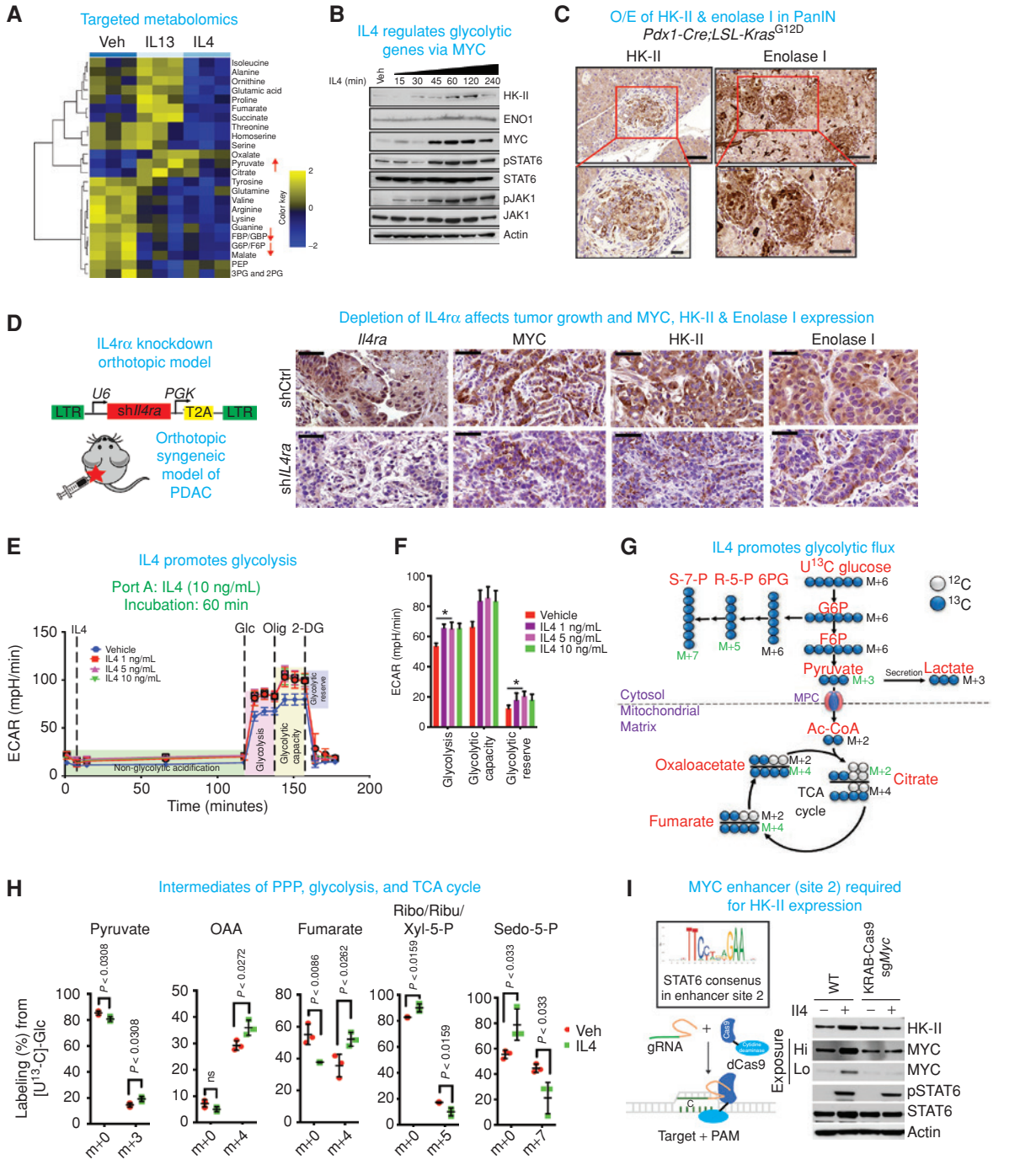

Figure 4. IL4/IL13 upregulates MYC to promote metabolic reprogramming. **A,** Heat map of those metabolites that were significantly and consistently changed upon treatment of IL4 or IL13 in two iKRAS* cell lines as determined by targeted LC/MS-MS. Cells were treated with IL4 or IL13 for 1 hour, at which point metabolite levels were measured from triplicates for each treatment condition. The averaged ratios of differentially regulated metabolites are represented in the heat map (differential FDR < 0.25). Arrows indicate metabolites involved in glucose metabolism that were regulated upon IL4 or IL13 treatment. **B,** Immunoblot analysis for HK-II, enolase I, MYC, pSTAT6, STAT6, pJAK1, and JAK1 of cells treated with IL4 (10 ng/mL) for indicated times. β-actin acts as a loading control. **C,** IHC of HK-II and enolase I in preneoplastic mouse (*Pdx1-Cre;LSL-Kras*^{G12D}) pancreas. The bottom panels are magnified images of the boxed regions. Scale bars, 50 μm and 100 μm, respectively. **D,** Left, cartoon of syngeneic orthotopic tumor model, whose tissues were used for IHC analysis. Right, representative IHC showing IL4Rα, MYC, HK-II, and enolase I expression in syngeneic orthotopic tumor tissues comparing sh*Il4ra* versus shCtrl knockdown. Scale bar, 50 μm. **E,** Seahorse analysis for ECAR of cells treated with IL4 (1–10 ng/mL) for 1 hour. **F,** Quantification of the Seahorse data on the left. Results are shown as mean ± SEM. *P* values were calculated using Student *t* test. **G,** Diagram of glycolysis and TCA cycle. Blue circles indicate ^{13}C-labeled sites. Red label indicates metabolites measured using mass spectrometry. **H,** Percentage labelling of ^{13}C-labeled sites in metabolites indicated. Data are presented as mean ± SEM. $n = 4$. Two-tailed *t* test was used for all comparisons between two groups. **I,** Consensus sequence of STAT6-binding site on the *Myc cis*-regulatory element (top left). Schematic of KRAB-dCas9 (bottom left). Immunoblot showing loss of IL4 mediated regulation of MYC and HK-II upon binding of KRAB-dCas9 on the *Myc cis*-regulatory element, that blocks the binding of STAT6 to the consensus *cis*-element. Actin acts as a loading control. PAM, protospacer adjacent motif.

Published OnlineFirst February 11, 2020; DOI: 10.1158/2159-8290.CD-19-0297

in vivo metabolic pathway profile. Consistent with increased glycolysis upon IL4 or IL13 treatment, we observed increased expression of the glycolytic genes hexokinase II (HK-II), and enolase I (Fig. 4B). The strong expression of HK-II and enolase I is also observed in the epithelial compartment of premalignant tumor models, alluding to upregulation of specific glycolytic genes (Fig. 4C) which are known MYC targets. Knockdown of IL4Rα in syngeneic orthotopic tumors caused a decrease in MYC and a concurrent decrease in HK-II and enolase I expression (Fig. 4D; Supplementary Fig. S4A and S4B). Using the Seahorse glycolysis stress test, we further analyzed the glucose consumption rate upon addition of IL4 and IL13 and detected a substantial increase in extracellular acidification rate (ECAR), which is an indication of acidification of the media upon conversion of glucose to lactate, and a net increase in protons in the spent media (Fig. 4E and F). Moreover, ^{13}C-glucose (Glc) tracing analysis showed that IL4 reprograms the glycolytic pathway by diverting more glucose-carbon toward energy production via the TCA cycle and less toward the PPP. We saw an enrichment in ^{13}C-isotope labeling in glycolysis and TCA cycle intermediates such as pyruvate, fumarate, and oxaloacetate (OAA). There was a simultaneous decrease in ^{13}C-isotope labeling in PPP intermediates such as ribose-5-phosphate and sedoheptulose-7-phosphate (Fig. 4G and H). Together, these findings support the view that IL4 and IL13 drive energy production via glycolysis and the TCA cycle.

We further validated whether IL4 acts through MYC or directly regulates the metabolic enzymes HK-II and enolase I. To test this hypothesis, we have utilized a catalytically inactive Cas9 (dCas9) fused to transcriptional repressor/chromatin effector domains (KRAB) allowing silencing of a genomic region of interest. We designed small guide RNA (sgRNA) that would target the STAT6 binding site 2, as detected in the ChIP-seq, on the *Myc cis*-regulatory element approximately 350 kb upstream of the *Myc* promoter region. Immunoblot shows that upon silencing of the STAT6 binding region, IL4-mediated regulation of MYC and HK-II is lost; however, the baseline expression of MYC remains intact, indicating alternate regulation of baseline MYC and HK-II expression (Fig. 4I). Similarly, using ruxolitinib, a JAK1-specific inhibitor, shows that upon inhibition of JAK1–STAT6 signaling, the IL4-mediated upregulation of MYC and HK-II is abolished (Supplementary Fig. S4C).

The Tumor Microenvironment Supplies IL4 and IL13

As IL4 and IL13 drive cancer-cell proliferation *in vivo* in our model, we sought to identify the source of these cytokines in the TME. IHC confirmed elevated IL4 and IL13 in KRAS*-On tumors compared with KRAS*-Off tumors or normal pancreas (Supplementary Fig. S5A). IL4 and IL13 are known to be secreted primarily by Th2-polarized CD4$^+$ T cells and to a lesser extent by mast cells, eosinophils, and stromal cells (30). The Th2 cells secrete IL4 and IL13 in a paracrine fashion, polarizing additional naïve CD4$^+$ T cells to Th2 type (31). Importantly, flow cytometry analysis showed that 40% to 60% of the live cells in the PDAC tumor were CD45$^+$ cells, of which 18% to 20% were CD3$^+$ cells and a majority of those were CD4$^+$ cells (Fig. 5A; Supplementary Fig. S5B–S5D). Next, mass cytometry by time-of-flight (CyTOF) was used to conduct a comprehensive immune profile of mouse PDAC tumors (on doxycycline for 12 weeks) and compare these profiles with those of normal pancreas and spleen (Fig. 5B; Supplementary Fig. S5E). Correspondingly, using multiplexed imaging mass spectrometry (iMC), human PDAC tissues also showed significant infiltration of CD4$^+$ T cells (Fig. 5C and D). These findings are consistent with recent reports that antitumor immune response is dependent on the presence of the right proportion of T effector (Th1 and CD8$^+$) cells versus tumor-promoting T (Treg, Th2, Th17) cells (10, 32). Expression of the transcription factors Tbet and GATA3 is used for molecular subtyping of Th1 cells and Th2 cells, respectively (33). Molecular characterization of the specific type of infiltrating CD4$^+$ T cells shows that most infiltrating CD4$^+$ T cells were GATA3$^+$ Th2 cells and only a small fraction were Tbet$^+$ Th1 cells (Fig. 5E and F; Supplementary Fig. S5F). Single-cell analysis of low- and high-grade intraductal papillary mucinous neoplasm (IPMN) and PDAC patient samples revealed CD4$^+$ T-cell infiltration and that a higher percentage of the CD4$^+$ T cells are GATA3$^+$ Th2 subtypes compared with Tbet$^+$ Th1 cells (Fig. 5G and H; Supplementary Fig. S5G).

Given the paucity of T cells in the TME of advanced PDAC and that KRAS mutational activation is an early event in PDAC tumorigenesis, we also assessed whether Th2 cells infiltrate during very early stages of the neoplastic process and potentially cooperate with KRAS* to drive tumorigenesis. We utilized the *Pdx-Cre;LSL-Kras*^{G12D} model, which generates ADM and PanIN lesions at 3 to 6 months of age; these neoplasms rarely progress to advanced malignancy following a long latency (34). IL4rα and IL13rα expression as well as activated STAT6 and elevated MYC levels were readily detected in the *Kras*^{G12D}-expressing neoplastic cells (Fig. 6A)—findings consistent with a potential role of IL4 and IL13 during early stages of tumorigenesis. Also, these PanIN-like lesions were infiltrated by CD4$^+$ T cells, which were also mostly Th2 type (GATA3$^+$; Fig. 5F; Supplementary Fig. S5F) as the GATA3:Tbet ratio was skewed toward the Th2 phenotype. On the basis of these findings, we speculated that infiltrating Th2 cells

Figure 5. The TME supplies IL4 and IL13. **A,** Quantification of total CD3$^+$, CD8$^+$, and CD4$^+$ populations in iKRAS* tumor compared with normal pancreas using flow cytometry. Cell populations were identified as T cells (CD45$^+$CD3e$^+$), CD4$^+$ T cells (CD45$^+$CD3e$^+$CD8$^-$CD4$^+$), CD8$^+$ T cells (CD45$^+$CD3e$^+$CD8$^+$CD4$^-$). **B,** viSNE analysis of CyTOF data of immune cells from tumor, colored by relative expression of CyTOF markers, with populations indicated as CD45$^+$, F4/80$^+$, CD4$^+$, and CD8$^+$. Total CD3$^+$ cells, tumor cells, and macrophage populations are circled. **C,** Representative images of two different ROI of multiplexed imaging (iMC) showing staining for E-cadherin, αSMA, CD4, CD8a, and CD68. White asterisks indicate CD4$^+$ T cells. **D,** viSNE plot of population analysis of iMC image (Fig. 5C). Shown are quantification of all events, CD45, E-cadherin, CD3, CD4, and CD8. **E,** Quantification of GATA3 and Tbet staining based on the IHC staining in PanIN model. ***, $P < 0.001$ **F,** Representative H&E and immunofluorescence images of PanINs stained with DAPI, GATA3, CD4. Right-most panel shows merged image of CD4 and GATA3. **G,** *t*-SNE plot of single-cell analysis (scRNA-seq) on IPMN and PDAC human tumor samples followed by digital microdissection of T cells to analyze the presence of various T-cell subtypes. Annotated colors represent lesion of origin of the respective T cells. **H,** Quantification of single-cell data (left) showing GATA3$^+$ and Tbet$^+$ CD4$^+$ T cells in human IPMNs (low and high grade) and PDAC samples.

Published OnlineFirst February 11, 2020; DOI: 10.1158/2159-8290.CD-19-0297

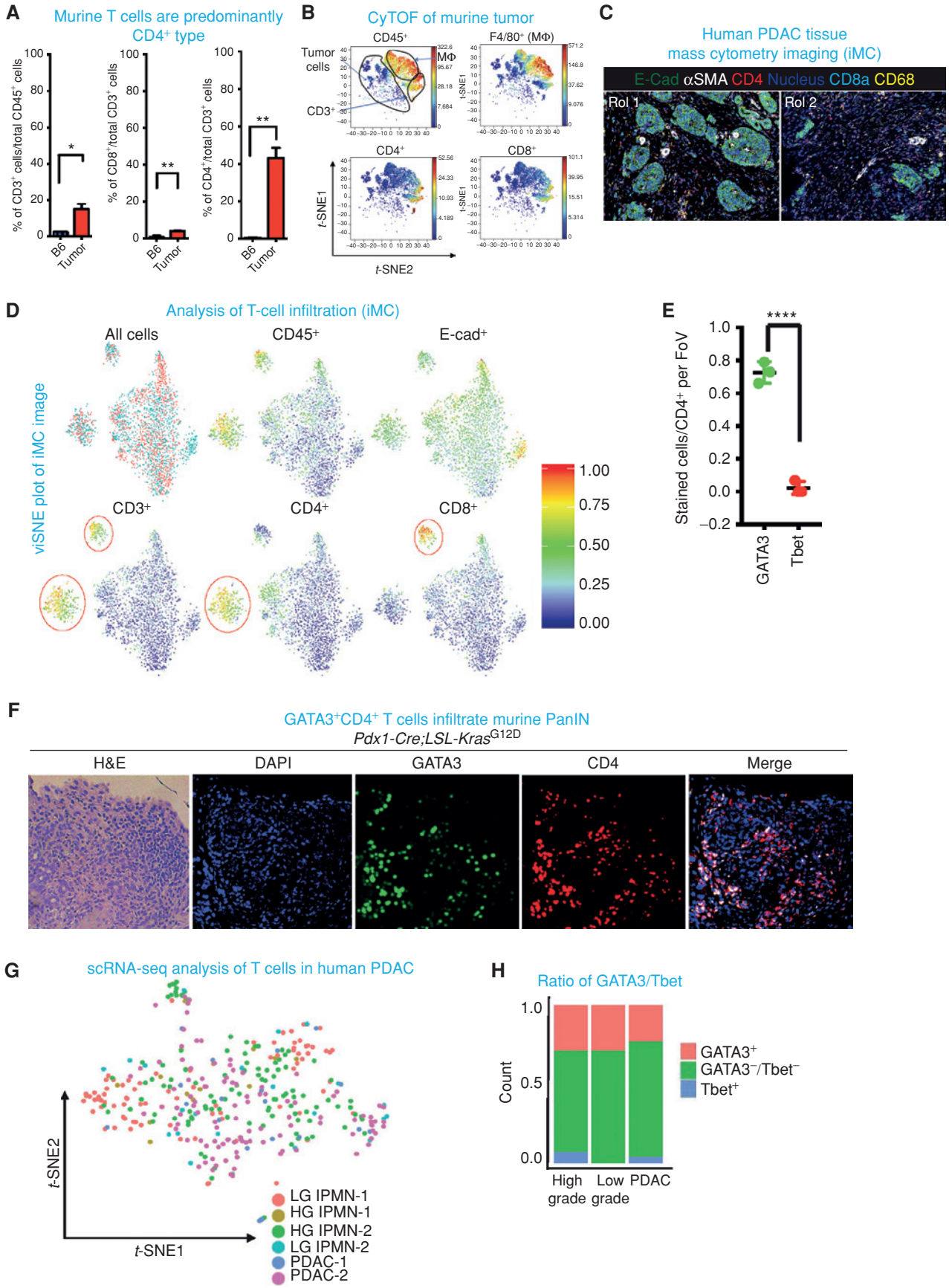

Published OnlineFirst February 11, 2020; DOI: 10.1158/2159-8290.CD-19-0297

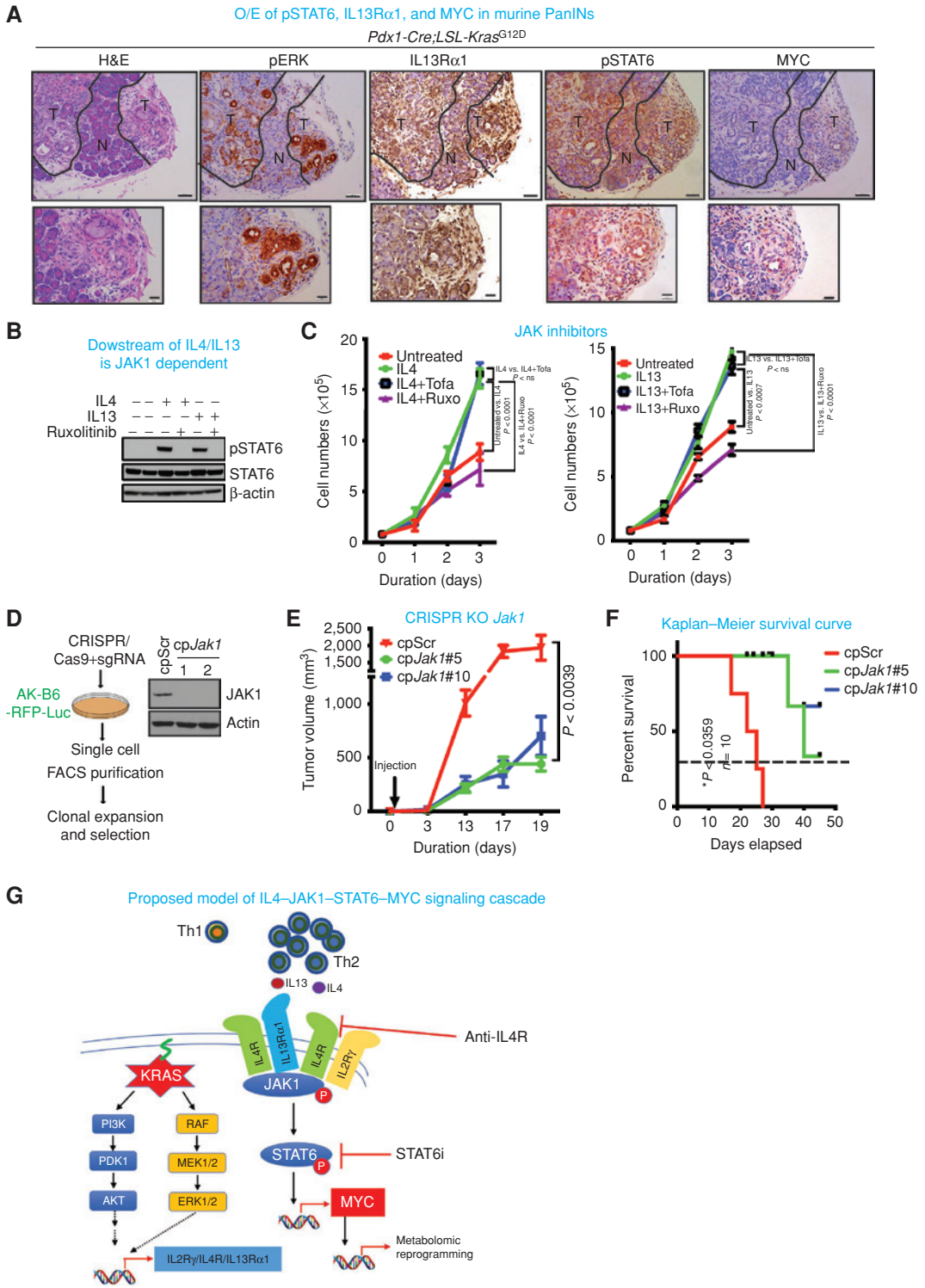

Figure 6. JAK1–STAT6 pathway promotes cancer cell proliferation and tumor growth. **A,** Representative H&E and IHC analysis of pERK, IL13Rα1, pSTAT6, and MYC in the preneoplastic pancreas. The bottom panels are amplified images of those above. Scale bars, 100 μm (top) and 50 μm (bottom). Representative luciferase images of comparing anti-HRP versus anti-IL4 ($n = 10$), imaged at day 4. **B,** Immunoblot of pSTAT6 and STAT6 upon treatment with IL4 or IL13 followed by treatment with ruxolitinib, a specific JAK1 inhibitor. β-actin acts as a loading control. **C,** Proliferation assay of iKRAS* cell lines upon treatment with IL4 or IL13 and followed by treatment with ruxolitinib (Ruxo; JAK1 inhibitor) and tofacitinib (Tofa; JAK2/3 inhibitor). **D,** Strategy for CRISPR/Cas9 knockdown of *Jak1* in mouse pancreas cell line. Immunoblot of JAK1 in two separate single clones of *Jak1* knockout cell lines. β-actin acts as a loading control. **E,** Tumor volume of transplanted tumor upon CRISPR/Cas9 knockout (KO) of *Jak1* compared with scrambled control ($n = 5$). **F,** Kaplan–Meier survival curves of mice transplanted with mouse tumor cell lines transfected with CRISPR/Cas9 knockout of *Jak1* or control cell lines ($n = 10$). **G,** Proposed model of IL4–JAK1–STAT–MYC signaling cascade that includes KRAS-mediated upregulation of IL4–IL2Rγ and IL4–IL13Rα1 receptors and infiltration of Th2 cells into the TME.

Published OnlineFirst February 11, 2020; DOI: 10.1158/2159-8290.CD-19-0297

contribute to pancreatic cancer initiation and progression. Accordingly, a regimen of 12 doses of anti-CD4 neutralizing antibody treatment of *Pdx-Cre;LSL-Kras*^{G12D} mice, starting at age 30 days, resulted in a decrease in size and number of PanIN lesions (Supplementary Fig. S6A). IHC staining of tissues derived from anti-CD4 treated mice showed a marked reduction in CD4$^+$ T cells in the vicinity of the smaller PanIN lesions; moreover, these lesions show reduced expression of PCNA, HK-II, and enolase I in the cancer cells (Supplementary Fig. S6B).

JAK1–STAT6 Pathway Promotes Cancer Cell Proliferation and Tumor Growth

To assess the molecular and biological impact of these IL4- and IL13-secreting Th2 cells on cancer cell signaling, we inhibited IL4- or IL13-mediated JAK–STAT pathway activation using ruxolitinib, a specific JAK1/2 inhibitor, and tofacitinib, a specific JAK3 inhibitor. Consistent with the role of JAK1 above, ruxolitinib inhibited STAT6 phosphorylation (Fig. 6B) and abolished IL4- and IL13-mediated growth stimulation of PDAC cells, whereas tofacitinib had no effect on the IL4- and IL13-mediated proliferation. (Fig. 6C). Similarly, JAK1 ablation by CRISPR/Cas gene editing (Fig. 6D) displayed markedly reduced tumor growth with *Jak1*-null cancer cells relative to unedited isogenic controls and increased survival (median survival 40 days; Fig. 6E and F). These genetic studies of inhibition of the JAK1 pathway support the role of the JAK1–STAT6 pathway in promoting PDAC growth. Of note, although anti-IL4 neutralizing antibody reduced tumor burden, these responses were not durable and the mice eventually succumbed to tumor recurrence (Supplementary Fig. S6C–S6E), suggesting that IL13 can complement IL4 function, and any attempt to target the Th2 signaling would likely require neutralizing both IL4 and IL13 cytokines. Alternatively, IL4R, the common receptor for IL4/IL13 signaling, may be an attractive target, as this intervention would block the signal emanating from both IL4 and IL13.

DISCUSSION

KRAS* plays a central role in PDAC initiation and maintenance through a variety of mechanisms involving its well-established autonomous cancer cell signaling functions. In this study, we show that a novel tumor-promoting function of KRAS* involves establishment of a paracrine circuit utilizing T-cell cytokines in the PDAC TME. Specifically, KRAS* is shown to regulate cytokine receptor expression in cancer cells and infiltrating T cells provide cytokines to activate these receptors, which in turn signal via JAK1–STAT6–MYC resulting in upregulation of glycolysis genes to support cancer cell metabolic reprogramming. Targeting components of this mutant KRAS–regulated pathway provides testable therapeutic targets for indirectly disrupting KRAS*-driven tumorigenesis.

Most work to date has focused on the classic role of IL4 in promoting tumor progression via activation of immune-suppressive macrophages (M2 polarization; refs. 13, 35), which in turn directly enhances cancer progression and metastasis via secretion of immunosuppressive molecules such as IL10 and TGFβ. This study, and the work of others (36), expands the role of IL4 in the context of KRAS*-driven PDAC through its promoting cancer cell proliferation via mutant KRAS–mediated upregulation of cytokine receptors such as IL4R, IL2Rγ, and IL13Rα1, which in turn enables IL4 and IL13 cytokine activation of the JAK1–STAT6–MYC pathway in cancer cells. MYC upregulation promotes cancer cell proliferation (37) and metabolic reprogramming characterized by increased glucose utilization as well as activation of the core glycolytic pathway (38). Importantly, MYC is required for metabolic reprogramming, as its loss has been shown to diminish expression of key metabolic genes required for maintaining the abovementioned metabolic pathways (1). In view of the MYC upregulation observed in our current study, we investigated its effect on metabolic genes. Following IL4 treatment, our work confirmed enhanced glycolytic pathway activity followed by an increase in TCA cycle intermediates and diminished PPP intermediates, a feature that is known to be attributed to MYC activation (38). This finding aligns convincingly with recent *in vivo* metabolic studies in various cancer models, where glucose is an important source of energy (39, 40).

Our findings emphasize the critical nature of TME-derived cytokines in shaping the metabolic landscape of cancer cells and further suggest that the absence of cytokines in the *in vitro* setting could account for the metabolic shift of cancer cells to glutaminolysis in cell culture (41). Overall, our prior work (1) and current study emphasize that KRAS and IL4 both can regulate MYC protein via distinct and reinforcing mechanisms. KRAS is known to regulate MYC protein stability via phosphorylation at site S62 (42), which inhibits proteasomal degradation of MYC. Moreover, in our prior work (1) we observed that glycolytic genes that are upregulated with KRAS* possess MYC binding elements in the promoter. In our current study, we extend our understanding of how KRAS regulates MYC by showing that KRAS also regulates a cytokine circuit that results in the transcriptional upregulation of MYC via activated STAT6 engagement of the upstream enhancer element of the MYC locus.

Factors secreted by cancer cells, especially cytokines such as GM-CSF, G-CSF, etc., have been long associated with the recruitment of leukocytes into the TME, which creates a tumor-permissive niche for cancer cells to thrive (43, 44). Of special interest are T cells, because of their therapeutic potential via immune checkpoint blockade inhibition (ICI). Unfortunately, the PDAC microenvironment lacks sufficient effector immune cells to mount antitumor immunity for any therapeutic benefit. At the same time, recent clinical studies suggest that lymphocyte function may remain an important determinant of clinical outcome, as evidenced by the expression of the inhibitory immune checkpoint genes that inversely correlate with survival. We speculate that the localization of lymphocytes in the stroma, but not in close proximity to cancer cells, might diminish their effector function and patient response to ICI therapy (10), yet still enable such immune cells to support tumor development via mechanisms elucidated in this study. That is, the current study emphasizes the presence of the various T-cell subtypes in the TME and highlights the possibility of distinct effects on tumorigenesis and cancer therapy responses. Generally, Th1 cells provide positive response to ICI such as with

Published OnlineFirst February 11, 2020; DOI: 10.1158/2159-8290.CD-19-0297

anti-CTLA4 therapy (45, 46) and induction of CD8$^+$ T-cell infiltration. Whereas polarization toward Th2 cells prevents tumor rejection and facilitates tumor growth (47), IL4 is one of the most abundant cytokines secreted by Th2 cells. Correspondingly, it is notable that patients with PDAC with predominantly Th2 (GATA3$^+$) polarized lymphoid infiltrate show reduced survival compared with tumors with higher levels of Th1 cells (47). Our data also revealed that infiltration of Th2 polarized cells is an early event, as evidenced by their prominence in PanIN lesions, well before the pancreas parenchyma has lost its cytoarchitecture. Earlier studies have shown that other CD4$^+$ T-cell subtypes, such as Th17 cells, can also infiltrate preneoplastic lesions (48, 49). Accordingly, we detect approximately 12% to 14% (data not shown) of CD4$^+$ Th17 cells in these early-stage lesions, although IL17RA expression in cancer cells is independent of KRAS* in our model.

A variety of mechanisms have been identified by which cancer cells reap the benefit of an immune-rich microenvironment. It is well established that pro- and/or anti-inflammatory cytokines and chemokines sourced from various immune (50–52) and stromal compartments (53) can shape the TME and ultimately dictate the trajectory of tumor progression. These cytokines and chemokines are in a constant tussle to promote or oppose host immune responses, which can lead to tumor progression, metastasis, and chemoresistance (54). In addition, although KRAS* is critical for all stages of tumorigenesis from initiation to metastasis, challenges surrounding anti–mutant KRAS therapeutics, coupled with murine studies showing bypass of KRAS* dependency (3, 55), underscore the need for alternative strategies targeting KRAS*-dependent circuitry to treat pancreatic cancer. The results of this study raise the possibility that targeting the IL4–IL4R–JAK1–STAT6 signaling cascade at the level of the dual neutralization of IL4/IL13 cytokines, IL4R receptor, JAK1, and/or STAT6 may provide such a therapeutic strategy (Fig. 6G). A phase II study, Ruxolitinib in Pancreatic Cancer Patients (RECAP), showed the median overall survival (OS) was significantly greater with ruxolitinib versus placebo. In a follow-up trial, two randomized, phase III studies, JANUS 1 and JANUS 2, were conducted to evaluate ruxolitinib in combination with capecitabine in patients with advanced/metastatic pancreatic cancer. However, the studies were terminated following a planned interim futility/efficacy analysis of JANUS 1, because of lack of increase in OS (56). Overall, our study has provided an avenue to explore novel pancreatic cancer treatment based on the hallmarks of cancer that involve heterotypic collaborative interactions between cancer cells and the cells of the TME.

METHODS

Ethics Statement and Animal Modeling

All mouse manipulations were approved under MD Anderson Cancer Center's Institutional Animal Care and Use Committee. All animals were maintained in pathogen-free conditions and cared for in accordance with the International Association for Assessment and Accreditation of Laboratory Animal Care policies and certification. All surgeries were performed with isoflurane anesthesia. Analgesic was administered after surgery along with temperature-controlled postsurgical monitoring to minimize suffering. TetO_Lox-Stop-Lox-KrasG12D (tetO_KrasG12D), ROSA26-LSL-rtTA-IRES-GFP (ROSA_rtTA), p48-Cre, and LSL-Trp53 strains were described previously (1). Mice were back-crossed to the C57BL/6 background for more than eight generations to achieve a pure B6 mouse, and its purity and zygosity were validated by Charles River. Mice were maintained in pathogen-free conditions at MD Anderson Cancer Center (Houston, TX). Mice with spontaneous pancreas tumors were euthanized at designated time points for tumor collection. Owing to the internal location of these tumors, we used signs of lethargy, reduced mobility, and morbidity, rather than maximal tumor size, as a protocol-enforced endpoint.

Subcutaneous and Orthotopic Syngeneic Models

For all experiments, C57BL/6J (Stock 000664) mice, aged 4 to 6 weeks, were obtained from Jackson Laboratory unless otherwise mentioned. A 2 × 2 mm portion of the left abdomen was shaved to facilitate transplantation. Subcutaneous tumors were established by injection of 1×10^6 cells into the flanks of mice. Tumor length and width were measured every 4 to 5 days and the volume was calculated according to the formula: Volume = (4/3) × 3.14 × (length/2) × (length/2) × (width/2). These experiments were not randomized, and the investigators were not blinded to allocation during experiments and outcome assessment. No statistical method was used to predetermine sample size. The cohort sizes for the study were estimated on the basis of previous experience using similar mouse models that showed significance. Animals were euthanized for humane reasons when tumors were approximately 15 mm in diameter. Doxycycline was provided to the animals in the form of doxycycline water (doxycycline 2 mg/mL, sucrose 40 mg/mL) starting 2 days prior to transplantation. For orthotopic pancreas transplantation, mice were anesthetized using ketamine/xylazine. An incision was made in the left abdomen and the pancreas was gently exposed along with the spleen. Luciferase-expressing cells were slowly injected into the tail of the pancreas using a Hamilton syringe. Five microliters of cells (5×10^5) mixed with 5 μL Matrigel was injected. For the orthotopic model, animals were imaged (IVIS Spectrum, PerkinElmer) 2 days after surgery to assess successful implantation of the tumors. Only orthotopic tumors of similar luciferase intensity were used further for the study. These criteria were preestablished. Furthermore, the animals were luciferase-imaged to monitor the progress of the tumor at different time points. Doxycycline water treatment was started 2 days after transplantation. Owing to the internal location of the tumors, we used signs of lethargy, reduced mobility, and morbidity, rather than maximal tumor size, as a protocol-enforced endpoint.

In Vivo *Imaging*

Live *in vivo* imaging was performed at the Small-Animal Imaging Facility at MD Anderson Cancer Center. MRI was performed using a Bruker ICON. For bioluminescence imaging, animals were anesthetized with isoflurane, injected intraperitoneally with 3 mg of D-luciferin (Perkin Elmer), and imaged using IVIS Spectrum Imaging System (Perkin Elmer). The Living Image 4.7 software (Perkin Elmer) was used for analysis of the images post acquisition.

Human PDAC Primary Tumor Samples

Human PDAC samples were obtained from MD Anderson's Tissue Biobank. The samples were stained using the standard IHC protocol. The antibodies used were IL2Rγ (Sigma Prestige HPA046641); IL4R (Bioss bs2458R); Tbet/TBX21 (CST 132325); and CD4 (Abcam ab133616). The stained samples were imaged using Pannoramic 250 slide scanner, and data were analyzed by two independent

Published OnlineFirst February 11, 2020; DOI: 10.1158/2159-8290.CD-19-0297

pathologists using Pannoramic viewer software (3DHISTECH Ltd). Human studies were approved by MD Anderson's Institutional Review Board (IRB), and prior informed consent was obtained from all subjects under IRB protocol LAB05-0854.

Digital Microdissection of TCGA Datasets

Digital microdissection of TCGA datasets was done by analyzing the mRNA expression data. Pearson correlation analysis of RNA datasets was done by comparing KRAS expression with known T-cell signature genes (CD8, IL2Rγ, ICOS, GZMK). A significant positive correlation of KRAS with T-cell signature genes was considered as coexpression of the above genes in the same tissue compartment.

Gene Expression Profiling and Computational Analysis

Gene expression profiling was performed using Affymetrix Gene Chip Mouse Genome 430 2.0 Arrays. Complete gene expression profiles are available at the Gene Expression Omnibus at GSE53169. For detailed protocol of the analysis, refer to Ying and colleagues (1).

Transcriptomic Profiling by RNA-seq and qRT-PCR

RNA was isolated using TRIzol extraction followed by purification with the Qiagen RNeasy Kit as described previously (57). RNA-seq was performed by the Sequencing and Microarray Facility core at MD Anderson Cancer Center. Libraries were generated using Illumina's TruSeq Kit and were sequenced using the Illumina HiSeq2000 Sequencer. Raw read RNA-seq data were mapped to hg19 reference genome using Bowtie (58). The mapped reads were then assembled by Cufflinks (59) to generate a transcriptome assembly for each sample. After the assembly phase, Cufflinks quantified expression level of the transcriptome in each gene for each sample (i.e., FPKM, fragments per kilobase of transcript per million fragments mapped). For qRT-PCR, RNA samples were reverse-transcribed into cDNA using the High-Capacity cDNA Reverse Transcript Kit (Life Technologies). cDNA samples were subjected to qRT-PCR quantification in duplicate and performed with Power SYBR Green PCR Master Mix (Life Technologies) according to the product guides on an Agilent Mx3005P and Applied Biosystems AB7500 Fast Real Time machine.

The primer sequences used for real-time qRT-PCR are the following: KRAS (forward 5′ CAAGAGCGCCTTGACGATACA 3′, reverse 5′ CCAAG AGACAGGTTTCTCCATC 3′), ACTB (forward 5′ GGCTGTATTCCCC TCCATCG 3′, reverse 5′ CCAGTTGGTAACAATGCCATGT 3′), IL2Rγ (forward 5′ AATCTGAGTGAATCCCAGCTAGA 3′, reverse 5′ GATCTC TGTTGCTCCGGTACT 3′), IL13Rα1 (forward 5′ ATGCTGGGAAAA TTAGGCCATC 3′, reverse 5′ ATTCTGGCATTTGTCCTCTTCAA 3′), IL4Rα (forward 5′ TCTGCATCCCGTTGTTTTGC 3′, reverse 5′ GC ACCTGTGCATCCTGAATG 3′), GM-CSF (forward 5′ TCGTCTCTAA CGAGTTCTCCTT 3′, reverse 5′ CGTAGACCCTGCTCGAATATCT 3′), E-Cadherin (forward 5′ CAGTTCCGAGGTCTACACCTT 3′, reverse 5′ TGAATCGGGAGTCTTCCGAAAA 3′), ITGB6 (forward 5′ CAG GTCCGCCAAACTGAAGAT 3′, reverse 5′ TGTTGAGGTCGTCATC CATAGA 3′).

Single-Cell RNA-seq and Analyses

Preparation of fresh human pancreatic tissue and dissociation into single cells: For fresh tissues undergoing single-cell transcriptomic analysis, a total of 6 patients were recruited at MD Anderson Cancer Center (MDACC) and University of Pittsburgh Medical Center (Pittsburgh, PA). Patients gave written informed consent to MDACC's banking protocol (Lab00-396), which included consent to provide leftover tissue for future analysis. Tissues were distributed for single-cell RNA-seq under MDACC's protocol PA15-0014 for use/analysis. All work was done following IRB approval at both institutions (PA15-0014, Lab08-0098, Lab05-0080, and Lab00-396). Following resection, pancreatic tissue was delivered to the laboratory on ice and dissociated into single-cell suspensions as described previously (60).

Single-cell transcriptomic amplification and library prep was performed using the SureCell WTA 3′ Library Prep Kit for the ddSEQ System and as described previously. Quality analysis and quantification of cDNA libraries was performed on an Agilent 2200 Tapestation system (Tapestation) using a High Sensitivity D5000 screentape (Agilent). Libraries were sequenced using a NextSeq 500 High Output Kit (Illumina). For a detailed protocol of sample preparation and analysis, refer to Bernard and colleagues (60). Digital microdissection of single barcoded cells determined to be lymphocytes from overall tumor cell population samples was performed on the basis of expression of CD45 and CD3 of individual cells. Location of single cells representing gene expression of interest was visualized on a dimensional reduction plot utilizing FeaturePlot. All *t*-SNE and heat maps were run in R v3.4.2.

Reagents, Drugs, Neutralizing Antibodies, and Chemicals

Ruxolitinib and tofacitinib were purchased from Selleckchem. ^{13}C- and ^{15}N-labeled isotopes were purchased from Cambridge Isotope Laboratories. Monoclonal neutralizing antibodies for *in vivo* experiments were obtained from BioXcell. For immune checkpoint blockade and IL4-neutralizing antibody treatment, anti-CD4 (clone GK1.5, BioXcell, BE0003-1) and anti-IL4 (clone 11B11, BioXcell, BP0045) antibodies or their respective horseradish peroxidase (HRP)–IgG controls were intraperitoneally administered at 200 μg per injection two times per week.

CyTOF and Imaging Mass Cytometry

Metal-labeled antibodies against cell-surface markers were purchased from Fluidigm. Pancreas tumor single cells were isolated using the Mouse Tumor Dissociation Kit (catalog no. 130-096-730, Miltenyi Biotec). Cells from spleen were isolated by mincing with a 5-mL syringe plunger against a 70-μm cell strainer into a 60-mm dish with RPMI medium containing 10% FBS. The cells were depleted of erythrocytes by hypotonic lysis. Peripheral blood (100 μL) was drawn using retro-orbital bleeding and depleted of erythrocytes by hypotonic lysis. Next, tumor, spleen, or blood cells were incubated with CD16/CD32 antibody (clone 2.4G2, BD Biosciences) to block FcγR binding for 10 minutes then with antibody mix for 30 minutes at room temperature. Cells were washed once and incubated with MAXPAR Nucleic Acid Intercalator-^{103}Rh (catalog no. 201103A, Fluidigm) for 20 minutes for viability staining. Cells were fixed with 1.6% formaldehyde for 1 hour and incubated with MAXPAR Nucleic Acid Intercalator-Ir (catalog no. 201192A, Fluidigm) at 4°C overnight to stain the nuclei. The samples were analyzed with CyTOF instrument (Fluidigm) in the Flow Cytometry and Cellular Imaging Core Facility at MD Anderson Cancer Center. Data were analyzed with FlowJo (Tree Star) and viSNE (61).The following markers were used to define different immune populations: Ly6G 139La (clone RB6-8C5), CD4 145Nd (clone RM4-5), CD45 147Sm (clone 104), CD11b 148Nd (clone M1/70), CD3e 152Sm (clone 145-2C11), Ly6c 162Dy (clone HK1.4), and CD8 146Nd (clone 53-6.7).

For iMC imaging, formalin-fixed, paraffin-embedded slides were processed similar to IHC samples. A cocktail of the following rare earth metal labeled antibodies was used: CD4 156Gd (clone EPR6855), SMA 141Pr (clone 1A4), CD68 159Tb (clone KP1), CD8a 162Dy (clone D8A8Y), E-Cadherin 158Gd (clone 24E10).

Flow Cytometry

Single cells for flow cytometry were obtained as described above for CyTOF. Fluorochrome-conjugated antibodies against CD45 (clone 30-F11), CD11b (M1/70), Gr-1 (RB6-8C5), and Ly6C (HK1.4) were purchased from eBiosciences. Antibody against Ly6G (1A8), CD4

Published OnlineFirst February 11, 2020; DOI: 10.1158/2159-8290.CD-19-0297

(GK1.5), CD3 (145-2C11), CD8 (53-6.7), Tbet (4B10), IL17RB (9B10), and GATA3 (16E10A23) was purchased from BioLegend. Primary cells from mice were isolated with the same methods as in CyTOF. To assess cell viability, cells were incubated with Ghost dye violet (Tonbo Biosciences) prior to FACS analysis. All samples were acquired with the LSRFortessa analyzer (Becton Dickinson) and analyzed with FlowJo software (Tree Star).

ChIP-seq

ChIP was performed as described previously (62) using STAT6 antibody (Cell Signaling Technology, 5397). Briefly, 5 μg rabbit IgG (Santa Cruz Biotechnology) or STAT6 antibody was incubated with Protein A Dynabead magnetic beads (Invitrogen) for 4 hours, followed by extensive washing to remove unbound antibody. Antibody beads were then added to the chromatin and incubated overnight.

Cell Culture and Establishment of Primary PDAC Lines

All the human cell lines (Hs766T, BxPc3, Patu8988T, and Patu8902) used in this study were purchased from ATCC, used below passage 25, and continuously cultured in 100 U/mL penicillin and 100 U/mL streptomycin. The cell lines were authenticated by short tandem repeat profiling at the Institute for Applied Cancer Sciences, MD Anderson Cancer Center. The Patu8988T, Hs766T, and Patu8902 cell lines were routinely cultured in DMEM with 10% FBS (Invitrogen). BxPc3 cell lines were routinely cultured in RPMI 1640 (Invitrogen) with 10% FBS. Primary mouse cell lines were established in the laboratory (AK-B6, AK192, HY6468, PJAK4217, PJAK4298) as described previously (34) and were routinely cultured in RPMI 1640 (Invitrogen) 10% FBS (Invitrogen). For inducible *KRAS*-derived cell lines, 1 μg/mL of doxycycline was directly added to the media. For metabolic and metabolomic assays, 10% dialyzed FBS (Atlanta Biologicals Inc.) was used. The cell lines were *Mycoplasma* free, based on tests done monthly in the laboratory using Lonza's MycoAlert Mycoplasma Detection Kit assays with confirmatory tests by PCR-based assays.

Organoid Culture and Treatment

Pancreas organoids were cultured according to the manufacturer's protocol and using PancreaCult Pancreas Organoid media (StemCell Technology). Briefly the pancreas was isolated, followed by mechanical and enzymatic dispersion. The isolated tissue clusters were then filtered through a 70-μm filter and embedded in Matrigel (63). The Matrigel was layered with PancreaCult media supplemented with 100 IU/mL penicillin and 100 μg/mL streptomycin (Invitrogen), 10 μmol/L Rho associated protein kinase (ROCK) inhibitor (StemCell Technology). Organoids were cultured and passaged every 5 days. For IHC, organoids were harvested and fixed in formalin followed by encapsuling in histogel and embedded in paraffin. The paraffin-embedded sections were stained using standard protocol for the following primary antibodies: DCLK1 (Abcam ab31704); Pan-CK (Novus Biologicals Inc. nbp2-29429); and PCNA (Abcam ab92552).

shRNA and CRISPR/Cas9 Knockdown

shRNA knockdown was performed as described previously (64). We screened 3 to 5 hairpins targeting the gene of interest and found three independent sequences that reduced mRNA levels by >60%. The shRNA sequences were as follows: *Il2rg* 5′ CCGGCCCTGATCTTTGTGTACTGTTCTCGAGAACAGTACACAAAGATCAGGGTTTTTG 3′ (TRCN0000068113) and 5′ CCGGGCTGTACAGAAGCTAAACCTACTCGAGTAGGTTTAGCTTCTGT ACAGCTTTTTG 3′ (TRCN0000068117); *Il4ra* 5′ CCGGCCTACACTACAGGCTGATGTTCTCGAGAA CATCAGCCTGTAGTGTAGGTTTTTG 3′ (TRCN0000068188) and 5′ CCGGCCTGGAATAACCT GTACCCATCTCGAGATGGGTACAGGTTATTCCAGGTTTTTG 3′ (TRCN0000068189). A nontargeting shRNA (shCtrl) was used as a control. The shRNA-expressing pLKO.1 vector was introduced into cancer cell lines by lentiviral infection. Recombinant lentiviral particles were produced by transient transfection of 293T cells following a standard protocol. Briefly, 10 μg of the shRNA plasmid, 5 μg of psPAX2, and 2.5 μg of pMD2.G were transfected using polyethylenimine (1 μg/μL, Polysciences #23966-2) into 293T cells plated in a 100-mm dish. Viral supernatant was collected 72 hours after transfection, centrifuged to remove any 293T cells, and filtered (0.45 μm). For transduction, viral solutions were added to cell culture medium containing 4 μg/mL polybrene; 48 hours after infection, cells were selected using 2 μg/mL puromycin and tested for gene depletion by qRT-PCR or immunoblotting. For CRISPR knockdown of *Jak1*, sgRNAs were purchased from Sigma (Sanger CRISPR clones). The sgRNAs were cloned into U6-gRNA:PGK-puro-2A-tagBFP (Sigma Sanger Vector). The sg*Jak1* sequences targeting DNA regions: ATTTTAGCACAGAACGCCATGG and GACTTTCTATCTGTTGGACAGG. The plasmids were virally transduced into cell lines and the cells were puromycin-selected and FACS-sorted for single clones. The clones were validated by Western blot analysis for deletion of *Jak1*.

Immunoblotting and Antibodies

Media were removed and the cells were washed twice in ice-cold PBS, scraped, and collected as pellets after centrifugation at 1,700 × *g* for 5 minutes. The pelleted cells were incubated in RIPA buffer with proteinase and phosphatase inhibitors for 15 minutes. Lysates were then collected and centrifuged at 208,000 × *g* for 15 minutes at 4°C. Protein concentrations were measured using the DC Protein Assay Kit (Bio-Rad, catalog no. 5000111). SDS-PAGE and immunoblotting were performed as described previously in precast Bis-Tris 4% to 20% gradient gels (Invitrogen; ref. 64). The following antibodies were used: IL2Rγ (Abcam ab180698, bioss bs-2545R); IL13Ra1 (Abcam ab79277); pAKT-S473 (Cell Signaling Technology 9271); STAT1 (Cell Signaling Technology 9172); STAT3 (Cell Signaling Technology 4904); pSTAT3-S727 (Cell Signaling Technology 9134); pSTAT2-Y690 (4441); pSTAT5-Y705 (Cell Signaling Technology 9145); STAT6 (Abcam ab28829); STAT6 (Cell Signaling Technology); pSTAT6-Y641 (Cell Signaling Technology 56554); pSTAT5-Y694 (Cell Signaling Technology 4322); pSTAT5 (Cell Signaling Technology 9359); JAK1 (Cell Signaling Technology 3344); pJAK1-Tyr1034/1035 (Cell Signaling Technology 74129); JAK2 (Cell Signaling Technology 3230T); JAK3 (Cell Signaling Technology 8827); pJAK3 (Cell Signaling Technology 5031); HK-II (Cell Signaling Technology 2867); Enolase (Abcam ab155102); pERK-p44/42 (Cell Signaling Technology 4370); MYC (Cell Signaling Technology 5605); PIM3 (Abcam ab71321); and β-actin (Sigma-Aldrich, A2228).

IHC and Immunofluroscence

Harvested tissues were immediately fixed in 10% formalin overnight and embedded in paraffin. IHC was performed as described previously (62). Briefly, endogenous peroxidases were inactivated by 3% hydrogen peroxide. Nonspecific signals were blocked using 3% BSA, 10% goat serum in 0.1% Triton X-100. Tumor samples were stained with the following primary antibodies: IL2Rγ (Abcam ab180698, Bioss bs-2545R); Ki-67 (Vector Laboratories, VP-RM04); IL4R (Bioss bs2458R); MYC (Abcam ab32072); HK-II (Abcam ab209847); GATA3 (Cell Signaling Technology 5852); LDHA (Cell Signaling Technology 3582); IL13Rα1 (Abcam ab79277); JAK1 (Cell Signaling Technology 3344); pSTAT1-Y701 (Cell Signaling Technology 9167); pSTAT3-Y705 (Cell Signaling Technology 9145); STAT5 (Cell Signaling Technology 94205); STAT1 (Cell Signaling Technology 9172); IL4 (Abcam ab9622); IL13 (Abcam ab106732); CD45 (Abcam ab10558), CD4 (Abcam ab183685), and F4/80 (Abcam ab6640). After overnight incubation, the slides were washed and incubated with secondary antibody (HRP polymers, Biocare Medical) for 30 minutes at room temperature. The slides were washed three times and stained with

DAB substrate (Thermo Fisher Scientific). The slides were then counterstained with hematoxylin and mounted with mounting medium. For clinical samples, staining intensity of tissue sections was scored in a "blinded" manner by two independent pathologists.

Immunofluorescence slides were imaged with an Olympus Microscope and quantified with ImageJ.

Glycolytic Capacity

Cells were plated into XF Cell Culture Microplates (Seahorse Bioscience) overnight at 37°C and 5% CO_2. The next day, cells were treated with IL4 and/or IL13 for 1 hour. To measure oxygen consumption rate and ECAR, media were replaced in the Seahorse microplates with assay medium free of sodium bicarbonate and FBS, and the plate was incubated in a CO_2-free incubator for 1 hour at 37°C. Oligomycin, FCCP, and rotenone were sequentially injected at a final concentration of 2 μg/mL, 1 μmol/L, and 1 μmol/L, respectively. Experiments were run using an XF analyzer, and raw data were normalized with total protein measured in each well of the microplate.

Isotope Labeling and Profiling by Targeted Mass Spectrometry

Glucose-free RPMI media were supplemented with 10% dialyzed serum and 12 mmol/L U-^{13}C-glucose (Cambridge Isotope Labs). For glucose-flux analysis, cells were maintained in glucose-free RPMI media overnight. The next day, the media were replaced with U-^{13}C-glucose-containing media.

For metabolite collection, media from biological triplicates (in 10-cm dishes at 70% confluence) was fully aspirated, and the cells were snap-frozen by the addition of liquid nitrogen. For metabolic extractions, 1 mL of 50% (v/v) methanol was added. Cells and the metabolite-containing samples were then collected into extraction vials. The cells were sonicated for 1 minute (30-second pulse twice) and mixed with 450 μL of ice-cold chloroform and vortex mixed in a Multi-Tube Vortexer for 10 minutes. The resulting homogenate was mixed with 150 μL of ice-cold water and vortexed again for 2 minutes. The homogenate was incubated at −20°C for 20 minutes and centrifuged at 4°C for 10 minutes to partition the aqueous and organic layers. The aqueous and organic layers were combined and dried at 37°C for 45 minutes in an Automatic Environmental Speed Vac system (Thermo Fisher Scientific). The extract was reconstituted in 500 μL of ice-cold methanol:water (50:50) and filtered through 3 kDa molecular filter (Amicon Ultracel -3K Membrane, Millipore Corporation) at 4°C for 90 minutes to remove proteins. The filtrate was dried at 37°C for 45 minutes in speed vac and stored at −80°C until mass spectrometry analysis. Prior to mass spectrometry analysis, the dried extract was resuspended in 50 μL of methanol:water (50:50) containing 0.1% formic acid and analyzed using MRM. Ten microliters were injected and analyzed using a 6490 QQQ triple quadrupole mass spectrometer (Agilent Technologies) coupled to a 1290 series HPLC system via selected reaction monitoring (SRM). Metabolites were targeted in both positive and negative ion mode; ESI voltage was +4,000 V in positive ion mode and −3,500 V in negative ion mode. Approximately 9 to 12 data points were acquired per detected metabolite. Samples were delivered to the MS via normal phase chromatography using a Luna Amino column (4 μm, 100A 2.1 × 150 mm, Phenomenex) at 400 mL/minute gradient spanning 80% B to 2% B over a 20-minute period followed by 2% B to 80% B for a 5-minute period and followed by 80% B for an 8-minute time period to reequilibrate the column. Buffer A was comprised of 5 mmol/L ammonium acetate (pH = 9.9) in water: acetonitrile. For ^{13}C-labeled experiments, SRMs were created for expected ^{13}C incorporation in various forms for targeted LC/MS-MS. To assess the validity of our method for calculating isotopomers, we determined the complete isotopomer distributions for each metabolite. Data analysis was performed in quantitative analysis and estimated the percent of isotopomer incorporation using the formula [% of Incorporation = $^{13}C/(^{13}C+^{12}C) \times 100$] and subtracted with the natural abundance.

Statistical Analysis

GraphPad Prism software was used to conduct the statistical analysis of all data, except for qPCR data where Microsoft excel was used. Data are presented as mean ± SD except for metabolic and metabolomic experiments where data are presented as mean ± SEM. All quantitative results were assessed by unpaired Student *t* test after confirming that the data met appropriate assumptions (normality and independent sampling). The Student *t* test assumed two-tailed distributions to calculate statistical significance between groups. Unless otherwise indicated, for all *in vitro* experiments, three technical replicates were analyzed. Sample size estimation was done taking into consideration previous experience with animal strains, assay sensitivity, and tissue collection methodology used. For clinical samples, IHC staining intensity of tissue sections was scored in a blinded manner by a pathologist. Animal survival impact was determined by the Kaplan–Meier analysis. $P < 0.05$ was considered statistically significant; the *P* values are indicated in the figures.

Data Availability Statement

Source data for the main article and Supplementary Data figures are provided in the online version of this article. All other data are available from the corresponding authors upon request.

Disclosure of Potential Conflicts of Interest

A. Maitra has ownership interest (including patents) in Thrive Earlier Detection and Cosmos Wisdom Biotechnology, and is a consultant/advisory board member at Lustgarten Foundation for Pancreatic Cancer Research Translational Advisory Group and Pancreatic Cancer Action Network Scientific and Medical Advisory Board. R.A. DePinho is a cofounder, director, and/or advisor at Tvardi Therapeutics, Asylia Therapeutics, and Nirogy Therapeutics. No potential conflicts of interest were disclosed by the other authors.

Authors' Contributions

Conception and design: P. Dey, A. Maitra, R.A. DePinho
Development of methodology: P. Dey, H. Wang, D. Chakravarti, B. Ghosh, N. Putluri
Acquisition of data (provided animals, acquired and managed patients, provided facilities, etc.): P. Dey, S. Chaurasiya, A. Strom, H. Wang, F. Cavallaro, V. Bernard, G. Genovese, P. Gulhati, J. Liu, P. Deng, T. Zhang, F. Carbone, H. Ying, X. Shang, N. Putluri
Analysis and interpretation of data (e.g., statistical analysis, biostatistics, computational analysis): P. Dey, J. Li, J. Zhang, H. Wang, W.-T. Liao, F. Cavallaro, V. Bernard, E.-Y. Yen, P. Gulhati, Q. Chang, N. Putluri, A. Maitra
Writing, review, and/or revision of the manuscript: P. Dey, H. Wang, V. Bernard, P. Gulhati, H. Ying, D.J. Spring, N. Putluri, A. Maitra, R.A. DePinho
Administrative, technical, or material support (i.e., reporting or organizing data, constructing databases): P. Dey, W.-T. Liao, P. Denz, T. Zhang, N. Putluri, Y.A. Wang
Study supervision: R.A. DePinho

Acknowledgments

We thank the MD Anderson core facilities supported by P30CA16672, including the Sequencing and Microarray Facility, Flow Cytometry and Cellular Imaging Core Facility; and S. Jiang and Z. Xu for assistance in maintenance of mouse colonies.

Published OnlineFirst February 11, 2020; DOI: 10.1158/2159-8290.CD-19-0297

The Metabolomic Core Facility at Baylor College of Medicine is supported by P30CA125123, CPRIT Proteomics and Metabolomics Core Facility (RP170005). In addition, this study was supported by NCI P01 CA117969 (to R.A. DePinho); NCI R01 CA225955 (to R.A. DePinho); DOD Postdoctoral Research Fellowship W81XWH-14-1-0429 (to P. Denz); K99/R00 grant 1K99 CA218891-01A1 (to P. Denz); U24 CA224020 (to A. Maitra); R01 CA218004 (to A. Maitra); R01 CA304969 (to A. Maitra). V. Bernard and D. Chakravarti were supported by the CPRIT Research Training Program (RP140106 and 170067). We thank Dr. Raghu Kalluri and colleagues for their critical review of the manuscript.

The costs of publication of this article were defrayed in part by the payment of page charges. This article must therefore be hereby marked *advertisement* in accordance with 18 U.S.C. Section 1734 solely to indicate this fact.

Received March 9, 2019; revised December 5, 2019; accepted February 6, 2020; published first February 11, 2020.

REFERENCES

1. Ying H, Kimmelman AC, Lyssiotis CA, Hua S, Chu GC, Fletcher-Sananikone E, et al. Oncogenic Kras maintains pancreatic tumors through regulation of anabolic glucose metabolism. Cell 2012;149:656–70.
2. Viale A, Pettazzoni P, Lyssiotis CA, Ying H, Sánchez N, Marchesini M, et al. Oncogene ablation-resistant pancreatic cancer cells depend on mitochondrial function. Nature 2014;514:628–32.
3. Kapoor A, Yao W, Ying H, Hua S, Liewen A, Wang Q, et al. Yap1 activation enables bypass of oncogenic Kras addiction in pancreatic cancer. Cell 2014;158:185–97.
4. Feig C, Gopinathan A, Neesse A, Chan DS, Cook N, Tuveson DA. The pancreas cancer microenvironment. Clin Cancer Res 2012;18:4266–76.
5. Clark CE, Hingorani SR, Mick R, Combs C, Tuveson DA, Vonderheide RH. Dynamics of the immune reaction to pancreatic cancer from inception to invasion. Cancer Res 2007;67:9518–27.
6. Steele CW, Jamieson NB, Evans TRJ, McKay CJ, Sansom OJ, Morton JP, et al. Exploiting inflammation for therapeutic gain in pancreatic cancer. Br J Cancer 2013;108:997–1003.
7. Protti MP, De Monte L. Immune infiltrates as predictive markers of survival in pancreatic cancer patients. Front Physiol 2013;4:210.
8. Ino Y, Yamazaki-Itoh R, Shimada K, Iwasaki M, Kosuge T, Kanai Y, et al. Immune cell infiltration as an indicator of the immune microenvironment of pancreatic cancer. Br J Cancer 2013;108:914–23.
9. Vonderheide RH, Bayne LJ. Inflammatory networks and immune surveillance of pancreatic carcinoma. Curr Opin Immunol 2013;25:200–5.
10. Blando J, Sharma A, Higa MG, Zhao H, Vence L, Yadav SS, et al. Comparison of immune infiltrates in melanoma and pancreatic cancer highlights VISTA as a potential target in pancreatic cancer. Proc Natl Acad Sci U S A 2019;116:1692–7.
11. Bluestone JA, Mackay CR, O'Shea JJ, Stockinger B. The functional plasticity of T cell subsets. Nat Rev Immunol 2009;9:811–6.
12. Coussens LM, Zitvogel L, Palucka AK. Neutralizing tumor-promoting chronic inflammation: a magic bullet? Science 2013;339:286–91.
13. DeNardo DG, Barreto JB, Andreu P, Vasquez L, Tawfik D, Kolhatkar N, et al. CD4(+) T cells regulate pulmonary metastasis of mammary carcinomas by enhancing protumor properties of macrophages. Cancer Cell 2009;16:91–102.
14. Rajamani D, Bhasin MK. Identification of key regulators of pancreatic cancer progression through multidimensional systems-level analysis. Genome Med 2016;8:38.
15. Terabe M, Park JM, Berzofsky JA. Role of IL-13 in regulation of anti-tumor immunity and tumor growth. Cancer Immunol Immunother 2004;53:79–85.
16. Asao H, Okuyama C, Kumaki S, Ishii N, Tsuchiya S, Foster D, et al. Cutting edge: the common gamma-chain is an indispensable subunit of the IL-21 receptor complex. J Immunol 2001;167:1–5.
17. Ayars M, O'Sullivan E, Macgregor-Das A, Shindo K, Kim H, Borges M, et al. IL2RG, identified as overexpressed by RNA-seq profiling of pancreatic intraepithelial neoplasia, mediates pancreatic cancer growth. Oncotarget 2017;8:83370–83.
18. O'Shea JJ, Holland SM, Staudt LM. JAKs and STATs in immunity, immunodeficiency, and cancer. N Engl J Med 2013;368:161–70.
19. Berta MA, Baker CM, Cottle DL, Watt FM. Dose and context dependent effects of Myc on epidermal stem cell proliferation and differentiation. EMBO Mol Med 2010;2:16–25.
20. Schuhmacher M, Eick D. Dose-dependent regulation of target gene expression and cell proliferation by c-Myc levels. Transcription 2013;4:192–7.
21. Armelin HA, Armelin MCS, Kelly K, Stewart T, Leder P, Cochran BH, et al. Functional role for c-myc in mitogenic response to platelet-derived growth factor. Nature 1984;310:655–60.
22. Dang CV. MYC on the path to cancer. Cell 2012;149:22–35.
23. Koh CM, Gurel B, Sutcliffe S, Aryee MJ, Schultz D, Iwata T, et al. Alterations in nucleolar structure and gene expression programs in prostatic neoplasia are driven by the MYC oncogene. Am J Pathol 2011;178:1824–34.
24. Wang H, Mannava S, Grachtchouk V, Zhuang D, Soengas MS, Gudkov AV, et al. c-Myc depletion inhibits proliferation of human tumor cells at various stages of the cell cycle. Oncogene 2008;27:1905–15.
25. Cappellen D, Schlange T, Bauer M, Maurer F, Hynes NE. Novel c-MYC target genes mediate differential effects on cell proliferation and migration. EMBO Rep 2007;8:70–6.
26. Yuneva M, Zamboni N, Oefner P, Sachidanandam R, Lazebnik Y. Deficiency in glutamine but not glucose induces MYC-dependent apoptosis in human cells. J Cell Biol 2007;178:93–105.
27. Shim H, Chun YS, Lewis BC, Dang CV. A unique glucose-dependent apoptotic pathway induced by c-Myc. Proc Natl Acad Sci U S A 1998;95:1511–6.
28. Mayers JR, Torrence ME, Danai LV, Papagiannakopoulos T, Davidson SM, Bauer MR, et al. Tissue of origin dictates branched-chain amino acid metabolism in mutant Kras-driven cancers. Science 2016;353:1161–5.
29. Davidson SM, Jonas O, Keibler MA, Hou HW, Luengo A, Mayers JR, et al. Direct evidence for cancer-cell-autonomous extracellular protein catabolism in pancreatic tumors. Nat Med 2017;23:235–41.
30. Choi P, Reiser H. IL-4: role in disease and regulation of production. Clin Exp Immunol 1998;113:317–9.
31. Bao K, Reinhardt RL. The differential expression of IL-4 and IL-13 and its impact on type-2 immunity. Cytokine 2015;75:25–37.
32. Carstens JL, Correa de Sampaio P, Yang D, Barua S, Wang H, Rao A, et al. Spatial computation of intratumoral T cells correlates with survival of patients with pancreatic cancer. Nat Commun 2017;8:15095.
33. Mikhalkevich N, Becknell B, Caligiuri MA, Bates MD, Harvey R, Zheng W-P. Responsiveness of naive CD4 T cells to polarizing cytokine determines the ratio of Th1 and Th2 cell differentiation. J Immunol 2006;176:1553–60.
34. Aguirre AJ, Bardeesy N, Sinha M, Lopez L, Tuveson DA, Horner J, et al. Activated Kras and Ink4a/Arf deficiency cooperate to produce metastatic pancreatic ductal adenocarcinoma. Genes Dev 2003;17:3112–26.
35. Wang H-W, Joyce JA. Alternative activation of tumor-associated macrophages by IL-4: priming for protumoral functions. Cell Cycle 2010;9:4824–35.
36. Bankaitis KV, Fingleton B. Targeting IL4/IL4R for the treatment of epithelial cancer metastasis. Clin Exp Metastasis 2015;32:847–56.
37. Bernard S, Eilers M. Control of cell proliferation and growth by Myc proteins. Results Probl Cell Differ 2006;42:329–42.
38. Dang CV. MYC, metabolism, cell growth, and tumorigenesis. Cold Spring Harb Perspect Med 2013;3:a014217.
39. Hosios AM, Hecht VC, Danai LV, Johnson MO, Rathmell JC, Steinhauser ML, et al. Amino acids rather than glucose account for the majority of cell mass in proliferating mammalian cells. Dev Cell 2016;36:540–9.

Published OnlineFirst February 11, 2020; DOI: 10.1158/2159-8290.CD-19-0297

40. Davidson SM, Papagiannakopoulos T, Olenchock BA, Heyman JE, Keibler MA, Luengo A, et al. Environment impacts the metabolic dependencies of Ras-driven non-small cell lung cancer. Cell Metab 2016;23:517–28.
41. Son J, Lyssiotis CA, Ying H, Wang X, Hua S, Ligorio M, et al. Glutamine supports pancreatic cancer growth through a KRAS-regulated metabolic pathway. Nature 2013;496:101–5.
42. Vaseva AV, Blake DR, Gilbert TSK, Ng S, Hostetter G, Azam SH, et al. KRAS suppression-induced degradation of MYC is antagonized by a MEK5-ERK5 compensatory mechanism. Cancer Cell 2018;34:807–22.
43. Bayne LJ, Beatty GL, Jhala N, Clark CE, Rhim AD, Stanger BZ, et al. Tumor-derived granulocyte-macrophage colony-stimulating factor regulates myeloid inflammation and T cell immunity in pancreatic cancer. Cancer Cell 2012;21:822–35.
44. Pylayeva-Gupta Y, Lee KE, Hajdu CH, Miller G, Bar-Sagi D. Oncogenic Kras-induced GM-CSF production promotes the development of pancreatic neoplasia. Cancer Cell 2012;21:836–47.
45. Ubaldi V, Gatta L, Pace L, Doria G, Pioli C. CTLA-4 engagement inhibits Th2 but not Th1 cell polarisation. Clin Dev Immunol 2003; 10:13–7.
46. Eagar TN, Turley DM, Padilla J, Karandikar NJ, Tan L, Bluestone JA, et al. CTLA-4 regulates expansion and differentiation of Th1 cells following induction of peripheral T cell tolerance. J Immunol 2004;172:7442–50.
47. De Monte L, Reni M, Tassi E, Clavenna D, Papa I, Recalde H, et al. Intratumor T helper type 2 cell infiltrate correlates with cancer-associated fibroblast thymic stromal lymphopoietin production and reduced survival in pancreatic cancer. J Exp Med 2011;208: 469–78.
48. Zhang Y, Zoltan M, Riquelme E, Xu H, Sahin I, Castro-Pando S, et al. Immune cell production of interleukin 17 induces stem cell features of pancreatic intraepithelial neoplasia cells. Gastroenterology 2018;155:210–23.
49. McAllister F, Bailey JM, Alsina J, Nirschl CJ, Sharma R, Fan H, et al. Oncogenic Kras activates a hematopoietic-to-epithelial IL-17 signaling axis in preinvasive pancreatic neoplasia. Cancer Cell 2014;25:621–37.
50. Landskron G, De la Fuente M, Thuwajit P, Thuwajit C, Hermoso MA. Chronic inflammation and cytokines in the tumor microenvironment. J Immunol Res 2014;2014:149185.
51. Dranoff G. Cytokines in cancer pathogenesis and cancer therapy. Nat Rev Cancer 2004;4:11–22.
52. Van Acker HH, Campillo-Davo D, Roex G, Versteven M, Smits EL, Van Tendeloo VF. The role of the common gamma-chain family cytokines in gammadelta T cell-based anti-cancer immunotherapy. Cytokine Growth Factor Rev 2018;41:54–64.
53. Sherman MH, Yu RT, Tseng TW, Sousa CM, Liu S, Truitt ML, et al. Stromal cues regulate the pancreatic cancer epigenome and metabolome. Proc Natl Acad Sci U S A 2017;114:1129–34.
54. Ying H, Dey P, Yao W, Kimmelman AC, Draetta GF, Maitra A, et al. Genetics and biology of pancreatic ductal adenocarcinoma. Genes Dev 2016;30:355–85.
55. Muzumdar MD, Chen P-Y, Dorans KJ, Chung KM, Bhutkar A, Hong E, et al. Survival of pancreatic cancer cells lacking KRAS function. Nat Commun 2017;8:1090.
56. Hurwitz H, Van Cutsem E, Bendell J, Hidalgo M, Li C-P, Salvo MG, et al. Ruxolitinib + capecitabine in advanced/metastatic pancreatic cancer after disease progression/intolerance to first-line therapy: JANUS 1 and 2 randomized phase III studies. Invest New Drugs 2018; 36:683–95.
57. Dey P, Jonsson P, Hartman J, Williams C, Ström A, Gustafsson J-Å. Estrogen receptors beta1 and beta2 have opposing roles in regulating proliferation and bone metastasis genes in the prostate cancer cell line PC3. Mol Endocrinol 2012;26:1991–2003.
58. Langmead B, Salzberg SL. Fast gapped-read alignment with Bowtie 2. Nat Methods 2012;9:357–9.
59. Trapnell C, Roberts A, Goff L, Pertea G, Kim D, Kelley DR, et al. Differential gene and transcript expression analysis of RNA-seq experiments with TopHat and Cufflinks. Nat Protoc 2012;7:562–78.
60. Bernard V, Semaan A, Huang J, San Lucas FA, Mulu FC, Stephens BM, et al. Single-cell transcriptomics of pancreatic cancer precursors demonstrates epithelial and microenvironmental heterogeneity as an early event in neoplastic progression. Clin Cancer Res 2019;25: 2194–205.
61. Amir E-AD, Davis KL, Tadmor MD, Simonds EF, Levine JH, Bendall SC, et al. viSNE enables visualization of high dimensional single-cell data and reveals phenotypic heterogeneity of leukemia. Nat Biotechnol 2013;31:545–52.
62. Dey P, Strom A, Gustafsson JA. Estrogen receptor beta upregulates FOXO3a and causes induction of apoptosis through PUMA in prostate cancer. Oncogene 2014;33:4213–25.
63. Sato T, Vries RG, Snippert HJ, van de Wetering M, Barker N, Stange DE, et al. Single Lgr5 stem cells build crypt-villus structures in vitro without a mesenchymal niche. Nature 2009;459:262–5.
64. Dey P, Baddour J, Muller F, Wu CC, Wang H, Liao W-T, et al. Genomic deletion of malic enzyme 2 confers collateral lethality in pancreatic cancer. Nature 2017;542:119–23.

Published OnlineFirst February 11, 2020; DOI: 10.1158/2159-8290.CD-19-0297

AACR American Association for Cancer Research

CANCER DISCOVERY

Oncogenic KRAS-Driven Metabolic Reprogramming in Pancreatic Cancer Cells Utilizes Cytokines from the Tumor Microenvironment

Prasenjit Dey, Jun Li, Jianhua Zhang, et al.

Cancer Discov 2020;10:608-625. Published OnlineFirst February 11, 2020.